

# Spatiotemporal wildfire modeling through point processes with moderate and extreme marks

Jonathan Koh\*  
 François Pimont<sup>†</sup> Jean-Luc Dupuy<sup>†</sup>  
 Thomas Opitz<sup>‡</sup>

November 22, 2021

## Abstract

Accurate spatiotemporal modeling of conditions leading to moderate and large wildfires provides better understanding of mechanisms driving fire-prone ecosystems and improves risk management. We study daily summer wildfire data for the French Mediterranean basin during 1995–2018. We jointly model occurrence intensity and wildfire sizes by combining extreme-value theory and point processes within a novel Bayesian hierarchical model. The occurrence component models wildfire ignitions as a spatiotemporal log-Gaussian Cox process. Burnt areas are numerical marks attached to points, and we consider fires with marks exceeding a high threshold as extreme. The size component is a two-component mixture varying in space and time that jointly models moderate and extreme fires. We capture non-linear influence of covariates (Fire Weather Index, forest cover) through component-specific smooth functions, which may vary with season. To reveal common drivers of different aspects of wildfire activity, we share random effects between model components to improve interpretability and parsimony without compromising predictive skill. Stratified subsampling of zero counts is implemented to cope with large observation vectors. We compare and validate models through predictive scores and visual diagnostics. Our methodology provides a holistic approach to explaining and predicting the drivers of wildfire activity and their associated uncertainties.

*Keywords:* Bayesian hierarchical model; Cox process; Extreme-value theory; Forest fires; Shared random effects.

---

\*Institute of Mathematics, EPFL, Station 8, 1015 Lausanne, Switzerland. Email: jonathan.koh@epfl.ch

<sup>†</sup>INRAE, URFM UR629, Site Agroparc, Domaine Saint Paul, 84914 Avignon, France. Emails: francois.pimont@inrae.fr, jean-luc.dupuy@inrae.fr

<sup>‡</sup>INRAE, BioSP, Domaine St. Paul, 228, Route de l'Aérodrome, 84914 Avignon, France. Email: thomas.opitz@inrae.fr

# 1 Introduction

Wildfires are defined as uncontrolled fires of combustible natural vegetation such as trees in a forest. Their activity usually shows seasonal cycles, as several conditions must coincide for their occurrence: the presence of combustible material as fuel, its easy flammability resulting from weather conditions such as droughts, and a trigger. Triggers include natural causes such as lightning, but the majority of occurrences in Europe are caused by human activity, either intentional (arson), neglectful (cigarette stubs) or accidental (agriculture).

Wildfires represent major environmental and ecological risks worldwide. They provoke many human casualties and substantial economic costs, and can trigger extreme air pollution episodes and entail important losses of biomass and biodiversity. While climate change may exacerbate their frequency and extent (Jones et al. 2020), wildfires themselves contribute an important fraction of global greenhouse gases that can accelerate climate change. To aid in wildfire prevention and risk mitigation, one must identify the factors contributing to wildfires and predict their spatiotemporal distribution. Prediction maps of various components of wildfire risk are relevant for the study of historical periods, for short-term forecasting and for long-term projections.

The study of wildfire activity has led to a large body of statistical and machine learning literature on providing methods for identifying risk factors and producing risk maps (Preisler et al. 2004, Xi et al. 2019, Pereira & Turkman 2019). Most studies focus on modeling either occurrence counts or sizes, the latter usually represented by the burnt areas of spatially and temporally contiguous wildfire events. In occurrence modeling, the spatial or spatiotemporal pattern of ignition points (or other representative points of separate wildfire events) can be analyzed with point process tools (Peng et al. 2005, Genton et al. 2006, Xu & Schoenberg 2011, Serra et al. 2013, Tonini et al. 2017, Pereira & Turkman 2019, Opitz, Bonneau & Gabriel 2020). Often, data are available as presence/absence or counts over dense spatial or spatiotemporal grids, or have been transformed to such representations to facilitate modeling and to harmonize different spatial-temporal scales of wildfire and predictor data such as weather conditions, land cover and land use.

Burnt area, a key measure of wildfire impact, provides a direct approximation of the biomass loss and greenhouse gas emissions, and it allows interpretation of impacts on ecosystem services such as biodiversity or clean air. Many univariate probability distributions have been explored for modeling fire sizes (e.g., Cumming 2001, Schoenberg et al. 2003, Cui & Perera 2008, Pereira & Turkman 2019). Empirical distributions are usually heavy-tailed, which is also the case with the wildfire data we consider in Mediterranean France. Heavy tails lead to a very small number of the most extreme wildfires accounting for a very large fraction of (aggregated) burnt area. There is no consensus on which parametric distribution family provides the best fit (Pereira & Turkman 2019). Distributions suggested by extreme-value theory, such as the generalized Pareto distribution (GPD) arising for threshold exceedances, have been studied (e.g., approaches by De Zea Bermudez et al. 2009, Mendes et al. 2010, Turkman et al.

2010, Pereira & Turkman 2019).

Joint statistical analyses of wildfire occurrence and sizes have been proposed and often use tools for marked point processes, where numerical marks represent burnt areas. Descriptive approaches (e.g., Tonini et al. 2017) characterize different regimes of wildfire activity (i.e., numbers, sizes, spatiotemporal autocorrelation) by taking into account weather, land cover, fire management and environmental factors. For explanatory and predictive modeling, Bayesian hierarchical models are useful and may include latent Gaussian components to allow for observation and estimation uncertainty, and to capture nonlinear influences of observed covariates. One may consider only categorical information (e.g., small and large wildfires) without attempting to model the continuous distribution of values; for example, Serra et al. (2014) construct a Bayesian spatiotemporal “hurdle” model to focus on occurrences of large wildfires. As to continuous distributions, Ríos-Pena et al. (2018) implement MCMC inference for zero-inflated Beta-regression to model the occurrence of wildfires in spatial units, with absence corresponding to zero-inflation, while positive area fraction covered by wildfires is captured through the Beta distribution. Joseph et al. (2019) estimate separate regression models with random effects for occurrence numbers in areal units and for sizes, and they study posterior predictive distributions for block maxima of wildfire sizes. Pimont et al. (2021) developed a marked spatiotemporal log-Gaussian Cox process model, called Firelihood, for daily data using extreme-value techniques for modeling the burnt areas as marks, applying the integrated nested Laplace approximation (INLA, Rue et al. 2009) for Bayesian inference. Their distribution of wildfire sizes over positive values is a mixture, of which each component is supported on the interval of a partition of the positive half-line; a GPD is specified for the most extreme interval. Weather information is included through a nonlinear effect of the Fire Weather Index (FWI, van Wagner 1977), constructed to yield high correlation with wildfire activity. The approach developed in this paper is motivated by shortcomings of the Firelihood model, and we consider the same study area in Southern France.

We propose important extensions to Pimont et al. (2021) and other works cited above. Since the heavy tails of burnt areas lead to a dominant influence of the most extreme wildfires, we focus on accurate modeling of the distribution of extreme wildfires, and its spatiotemporal variation. However, models constructed with only data of extreme wildfires would lead to high estimation uncertainty when inferring the complex spatiotemporal structures. Therefore, we propose joint estimation of extreme and non extreme wildfires, and the model borrows strength from non-extreme components for extreme components.

The complexity of the Firelihood model required separate estimation of the occurrence and size model components, thus hampering inferences exploiting stochastic interactions between the two components. Moreover, temporal stochastic structures in Firelihood were restricted to spatiotemporal variability of covariates, and to a two-level categorical effect to capture a decrease of wildfire numbers observed after the pivotal year of 2003, marked by exceptionally high wildfire activity events, may have led to improved wildfire prevention.

Simulated predictive distributions of wildfire activity for various divisions of the space-time domain did not appropriately capture some very extreme events, specifically the year 2003. In the present paper, we develop a more flexible spatiotemporal structure and data subsampling schemes for joint estimation and fully Bayesian inference of all components. We take care to achieve subsample sizes that allow running models on standard desktop computers, in contrast to often highly computer-intensive approaches in the literature (e.g., [Joseph et al. 2019](#), [Pimont et al. 2021](#), [Opitz, Bonneau & Gabriel 2020](#)) requiring high memory resources.

Here we use marked point processes defined over continuous space and time and extreme-value theory to represent the mechanisms leading to extreme wildfires exceeding a fixed high severity threshold for burnt areas. The point pattern of extreme fires can be viewed as a thinning of the full pattern, and we conduct threshold selection to identify a suitable threshold for applying the theoretically justified GPD to the threshold excesses.

We also advocate sharing spatial random effects that affect several model components simultaneously: the random effect is estimated for one response variable (e.g., wildfire counts) but we also include it with a scaling coefficient in other response variables (e.g., wildfire size exceedances). Sharing can be used as a tool to increase model parsimony, and it may offer new scientific insight ([Opitz, Bakka, Huser & Lombardo 2020](#)).

The FWI quantifies the influence of weather drivers on wildfire activity. [Pimont et al. \(2021\)](#) used a flexible nonlinear FWI effect but highlighted diminished predictive power of FWI depending on season. Therefore, we here propose a more sophisticated seasonal nonlinear FWI effect.

Predictive model validation is intricate because of heavy tails and high prediction uncertainty for individual wildfires, so customary validation scores, such as means of squared or absolute errors, are not useful. In addition to visual diagnostics, we tackle this through joint assessment of several numerical criteria, either through scores for binary data (e.g., Area under the Curve, [Fawcett 2006](#)) to assess the exceedance behavior over a range of severity thresholds, or through comparison of the distribution of probabilistic scores for continuous predictions, such as the scaled Continuous Ranked Probability Score ([Bolin & Wallin 2020](#)).

We estimate our marked log-Gaussian Cox process in a Bayesian setting using INLA ([Illian et al. 2012](#)) with Penalized Complexity (PC) priors for hyperparameters ([Simpson et al. 2017](#)). Gaussian process priors follow the Matérn covariance function, and we use the Stochastic Partial Differential Equation (SPDE) approach of [Lindgren et al. \(2011\)](#) for numerically efficient Gauss–Markov approximation.

In the remainder of the paper, we first describe and explore available data on wildfires and predictors in §2. We provide general background on extreme-value theory and point processes, and on how to combine them in a Bayesian hierarchical model using the INLA-SPDE method in §3. The specific hierarchical structure for the joint analysis of extreme and non-extreme wildfires is developed in §4. Estimation with subsampling of pixel-days without wildfire occurrences is detailed in §3.3. After a comparative analysis of models in §5,



we highlight interpretation of key findings and prediction of wildfire activity components in §6. We conclude with a discussion and outlook in §7.

## 2 Wildfire data

### 2.1 Prométhée wildfire database for Mediterranean France

Since 1973, wildfires occurring in the fire-prone French Mediterranean region have been recorded in the Prométhée database ([www.promethee.com](http://www.promethee.com)). Each wildfire occurrence is reported with its fire ignition cell in a  $2 \times 2\text{km}^2$  grid, day of detection and burnt area in hectare (ha). Inconsistent reporting was found for small wildfires, especially smaller than 1 ha, and we keep only data with reported burnt area larger than 1 ha; i.e., of escaped wildfires (Pimont et al. 2021) that could not be extinguished at an early stage. Like Pimont et al. (2021), we use the observation period 1995–2018, for which gridded weather reanalysis data (SAFRAN model of Météo France) and information on forested area are available.

Figure 1 illustrates the heavy tails in the distribution of burnt areas and strong spatial variability in numbers and sizes of wildfires. It also shows the contours of administrative areas (“départements”) in the study region. Small to moderately large wildfires strongly dominate the pie charts for wildfire counts, while large wildfires strongly dominate the pie charts of aggregated burnt area. Certain spatial patterns are similar in the distribution of numbers and sizes of wildfires (top and bottom display of Figure 1, respectively), but we also discern notable differences. For example, large wildfire numbers do not always entail large aggregated burnt areas, as can be seen for the Pyrénées-Orientales département in the southwest. The disparities among the two displays gives reason for modeling both wildfire numbers and sizes, as well as their interaction. Figure 2 (left panel) shows a histogram of burnt area values. The sum of burnt areas exceeding the empirical 99%-quantile is larger than the corresponding sum of the remaining wildfires.

### 2.2 Fire Weather Index and forest cover data

The SAFRAN model provides gridded weather reanalyses at 8km resolution. The joint influence of weather variables such as temperature, precipitation and wind speed on fire activity patterns is highly complex. Meteorological indices of fire danger have been constructed, such as the widely used unitless Fire Weather Index (FWI) that was originally defined for Canadian forests. Its values are often used for direct interpretation and risk mapping. Instead, we here study its relationship to components of fire risk, such as occurrence frequency and wildfire sizes. For our models, we preprocess SAFRAN data to daily FWI and use the SAFRAN grid by aggregating daily wildfire counts to its cells; Pimont et al. (2021) explain why this is sensible for this study area.

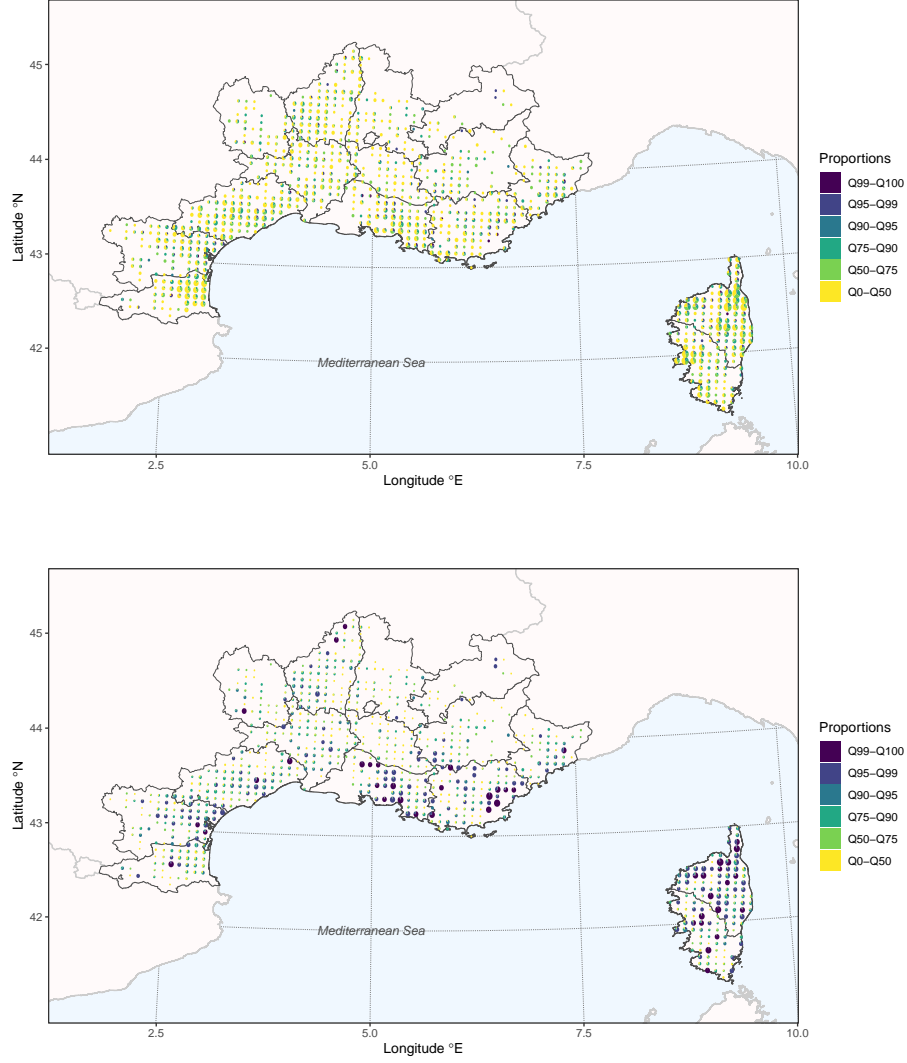


Figure 1: Maps of Prométhée data aggregated to the SAFRAN grid at 8km resolution. The pie charts in the grid cells are based on 6 wildfire size classes with boundaries given by empirical quantile levels 0, 0.5, 0.75, 0.9, 0.95, 0.99, 1 of all burnt areas (June–October). Top display: pie charts show relative count proportions over the six classes and have size increasing with increasing counts. Bottom display: pie charts show relative burnt area proportions and have size increasing with increasing aggregated burnt area.

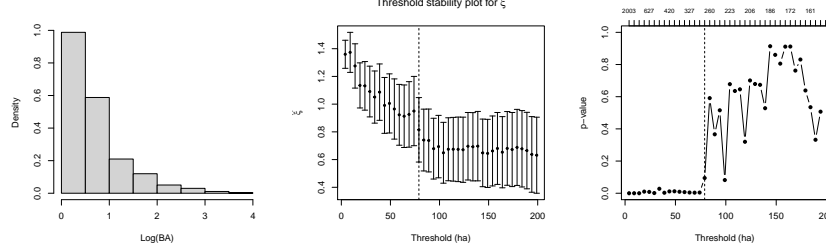


Figure 2: Burnt area distribution. Left: Histogram of burnt areas (ha) in base-10-logarithm ( $\log_{10}$ ). Middle: Parameter stability of the tail index. Right: p-values for testing the null hypothesis of a GPD distribution above the threshold; the tick labels on top indicate the number of fires above the given threshold.

Forest cover is another crucial explanatory variable. The study area hosts approximately 60% of forested areas or vegetation types that ignite easily (shrubland; other natural herbaceous vegetation). Wildfires do not propagate easily through the other available land cover types. We consider relevant fuel material through proportion covered by this vegetation in each SAFRAN grid cell (and day) based on CORINE Land Cover data (CLC). CLC dynamics are captured by linear temporal interpolation of several inventories. We refer to the resulting pixel-day predictor as forested area (FA), in %.

### 3 Methods for point patterns with extreme marks

#### 3.1 Extreme-value theory

Given a random variable  $X \sim F$  with distribution  $F$  satisfying mild regularity conditions, the generalized Pareto distribution (GPD) arises asymptotically for the positive excesses of  $X$  above a threshold increasing to  $x^* = \sup\{x : F(x) < 1\}$ . Therefore, given a large threshold  $u < x^*$ , the tail behavior of a wide class of random variables  $X$  can be approximated as

$$\Pr(X > x + u \mid X > u) \approx \text{GPD}_{\sigma, \xi}(x) = \begin{cases} (1 + \xi x / \sigma)_+^{-1/\xi} & \xi \neq 0, \\ \exp(-x / \sigma) & \xi = 0, \end{cases} \quad x > 0, \quad (1)$$

with shape parameter  $\xi \in \mathbb{R}$  and scale parameter  $\sigma = \sigma(u) > 0$ , where  $a_+ = \max(a, 0)$ . The shape parameter determines the rate of tail decay, with slow power-law decay for  $\xi > 0$ , exponential decay for  $\xi = 0$ , and polynomial decay towards a finite upper bound for  $\xi < 0$ . Writing  $p_{\text{exc}} = 1 - F(x)$  for the exceedance probability of  $X$  above  $u$ , we use (1) to approximate the cumulative distribution function  $F$  of  $X$  above the threshold  $u$  (Davison & Smith 1990) as

$$F(x) \approx 1 - p_{\text{exc}} \text{GPD}_{\sigma, \xi}(x - u), \quad x > u, \quad (2)$$

where  $\xi$ ,  $\sigma$  and  $p_{\text{exc}}$  are parameters to be estimated. We account for dependence and non-stationarity among observations by including auxiliary variables and Gaussian random effects into  $\sigma$  and  $p_{\text{exc}}$ . Nonstationarity in  $\xi$  is often hard to identify, and we therefore keep  $\xi$  stationary.

Based on (2), we model the conditional GPD of fire size excesses and  $p_{\text{exc}}$ . To explore the tail behavior of all fire sizes pooled together and choose an appropriate threshold  $u$ , we can use tools such as mean excess plots (see Supplement §8.2) or the following threshold stability plot of parameters, here considered for the GPD shape  $\xi$ , estimated by maximum likelihood for a range of increasingly high thresholds  $v_1 < \dots < v_m$ . We use multiple statistical tests (Northrop & Coleman 2014) to test the null hypotheses that the data come from a common truncated GPD on all intervals  $(v_k, v_{k+1})$ ,  $k = 1, \dots, m$ , where  $v_{m+1} = \infty$ . Using  $m = 40$  equidistant intervals of length 5ha for fire sizes, Figure 2 provides evidence that stability is reached above approximately the 95% quantile (79ha), with failure to reject the null hypothesis of  $\xi_k = \dots = \xi_m$  for intervals with  $v_k > 79\text{ha}$  and estimated shape  $\xi_k \approx 0.7$ .

Joseph et al. (2019) modeled fire sizes in the contiguous United States and concluded that the GPD leads to overestimation of extreme fire sizes. However, they fitted the GPD to the full distribution; Figure 2 shows that we would have obtained a very different value  $\hat{\xi} \approx 1.4$  for  $u = 1$ , which entails an extremely slow tail decay.

### 3.2 Mark-dependent thinning of point processes

We consider the point pattern of fire ignitions and burnt areas as a realization of a spatiotemporal marked point process; i.e., of a random count measure  $N$  that attributes value  $N(B) \in \{0, 1, 2, \dots\}$  to Borel sets  $B \subset \mathbb{R}^2 \times \mathbb{R}$ . We model the intensity function  $\lambda(x)$  of the point process in the observation window  $\mathcal{D} \subset \mathbb{R}^2 \times \mathbb{R}$ . It defines the expected number of points  $\mu(B)$  for any  $B \subset \mathcal{D}$  as

$$\mu(B) = \mathbb{E}N(B) = \mathbb{E} \sum_{i=1}^N 1(x_i \in B) = \int_B \lambda(x) \, dx.$$

We consider Poisson point processes characterized by the counts  $N(B) \sim \text{Pois}\{\mu(B)\}$ . With two types of points, such as non-extreme and extreme points, the point pattern is a superposition of the two single-type patterns:  $\lambda = \lambda_1 + \lambda_2$ . The points of a specific type, say type 2, can be obtained by thinning the full point pattern; i.e., by removing the points of other types (here type 1) using the thinning probability  $p(x) = \lambda_2(x)/\lambda(x)$ ,  $x \in \mathcal{D}$ . Extreme events, characterized as points  $x_i$  whose magnitude mark  $y_i$  exceeds a fixed high value  $u(x_i)$  are obtained by thinning the full point pattern. Given a point pattern  $\{x_1, \dots, x_N\}$ ,  $N \geq 1$ , we define variables  $E_i = \mathbb{I}\{y_i > u(x_i)\} \sim \text{Bernoulli}\{p(x_i)\}$ ,  $i = 1, \dots, N$ . With independent thinning (i.e.,  $E_i$  are mutually independent), a thinned Poisson process is again a Poisson process, and in more general settings the interaction structure remains the same (Chiu et al. 2013).

### 3.3 Spatiotemporal LGCPs

Log-Gaussian Cox processes (LGCPs) are Poisson processes with log-Gaussian intensity function  $\lambda(x)$ . Two major challenges arise for likelihood-based inference in LGCPs: (i) intensity functions are conceptually defined over continuous space; (ii) the Gaussian random effects lead to an intractable likelihood with no general closed-form expression. Challenge (ii) requires estimation techniques to handle latent variables; see §3.5. As to (i), without considering the marks, LGCPs have no general closed-form expression for their probability densities

$$(x_1, \dots, x_N) \mapsto \mathbb{E}_\lambda \exp \left( - \int_{\mathcal{D}} \lambda(x) \, dx \right) \prod_{i=1}^n \lambda(x_i), \quad (3)$$

where  $x = x(s, t)$  is a point in the space-time observation window  $\mathcal{D}$ . Different approximation strategies allow numerical computation of the integral  $\int_{\mathcal{D}} \lambda(x) \, dx$  for a given intensity function. We opt for discretizing the observation window using the SAFRAN grid, and assume that the intensity function does not vary within pixel-day grid cells. Conditional on  $\lambda$ , the number of points observed in a cell  $C_k$ ,  $k = 1, \dots, K$ , is Poisson distributed. Therefore, estimating the LGCP corresponds to performing a (mixed) Poisson regression with log-link:

$$N_k \stackrel{\text{ind}}{\sim} \text{Pois}(|C_k| \lambda_k), \quad \mathbb{E}[N_k \mid \lambda] = \lambda_k, \quad \log(\lambda_k) = \mu_k, \quad k = 1, \dots, K, \quad (4)$$

where  $|C_k|$  is the Lebesgue volume,  $\bigcup_k^K C_k = \mathcal{D}$  and  $C_{k_1} \cap C_{k_2} = \emptyset$  if  $k_1 \neq k_2$ . The linear predictor  $\mu_k$  can be additively composed of fixed and random effects. For space-varying random effects, we use the value at the center of the grid cell. Likelihood-based inference for latent Gaussian processes is often based on Laplace approximation (Tierney & Kadane 1986). In particular, the INLA framework assumes conditional independence of the observations given the latent Gaussian predictor and is thus well suited for LGCPs, where the Poisson observations  $N_k$  are conditionally independent given  $\mu_k$  (Illian et al. 2012, Opitz, Bakka, Huser & Lombardo 2020). Other approaches for numerically approximating the integral in (3) exist. Typically, they use appropriately weighted sums  $\sum_k \omega_k \lambda(\tilde{x}_k)$  with discretization points  $\tilde{x}_k$  and weights  $\omega_k > 0$ , which lead to variants of Poisson and logistic regression (e.g., the Berman–Turner 1992 device); see Baddeley et al. (2010).

### 3.4 Data aggregation and subsampling schemes

Spatiotemporal hierarchical modeling is notoriously computer-intensive due to large datasets and numerical challenges with covariances. With the R-INLA implementation (Rue et al. 2017), up to several hundred thousand observations can be handled. Stable inferences may require compromises with respect to the complexity of the latent model and the number of observations, which jointly determine the size and sparsity of the Gaussian precision matrices, which in turn influence computation times, memory requirements and well-conditioned numerical behavior. Even stronger restrictions arise with methods such as Markov

Chain Monte Carlo (MCMC) to achieve approximation quality comparable to INLA (Taylor & Diggle 2014, van Niekerk et al. 2019). Krainski et al. (2018, §8.4) develop strategies for LGCPs by aggregating the events to larger mapping units and lowering spatial-temporal resolution of random effects to decrease computation times, which, however, would impede modeling structures arising at small spatiotemporal scales.

Another way to cope with these issues is subsampling (Baddeley & Turner 2000, Rathbun et al. 2007, Tokdar & Kass 2010, Baddeley et al. 2010, Rathbun 2013, Baddeley et al. 2014, Raeisi et al. 2021), where the model is estimated using an appropriately reweighted subsample of data points, which keeps the loss of information small. Since maximum likelihood is equivalent to maximizing the empirical expectation of the log-density of observations, a subsampling scheme is appropriate if it ensures a faithful approximation of this expectation. Subsampling in likelihood-based estimation can be interpreted as importance sampling (Tokdar & Kass 2010): the original sample with observation weight unity is replaced by a subsample with typically larger observation weights. The theory for weighted subsampling goes back to Horvitz & Thompson (1952).

The Poisson intensities  $\lambda_k = \exp(\mu_k)$  ( $k = 1, \dots, K$ ) in (4) are the parameters to be estimated, and we need a subsample  $N_{k_j}$  with weights  $\omega_j$  ( $j = 1, \dots, J$ ) such that the subsample likelihood is close to the full density (3). The sample size  $K$  exceeds 5 million due to over 1000 daily-replicated spatial pixels. To enable R-INLA-based estimation, we devise a stratified subsampling scheme to reduce the number of observations by hundredfold. Observations  $N_k > 0$  are not subsampled since they are rare and highly informative; we keep them with each weight unity. For the zeroes, we link subsampling to Poisson additivity. The likelihood contribution  $\exp(-\lambda_k)^{\omega_k} = \exp(-\omega_k \lambda_k)$  with weight  $\omega_k \in \mathbb{N}$  is equal to the likelihood of the sum of  $\omega_k$  observations with count 0; the size of the initial sample is divided by the factor  $\omega_k$ . The predictors (covariates, random effects), and therefore of intensities  $\lambda_k$ , differ between different pixel-days  $k$  in our models, so Poisson additivity cannot be applied without additional approximations. However, the values of such predictors may often be very similar for cells located close in space and time, so we can limit the loss of information due to subsampling that preserves a representative coverage of space and time.

We partition our data by years and pixels and then apply subsampling within each partition. The subsample contains a fixed number of observations (here set to two) for each year-pixel combination. We thus obtain approximately 50,000 observations in the subsample, in line with the rule of thumb of Baddeley et al. (2014, 2015) that the subsample should be at least a factor four larger than the number of event points. The resulting models can be run on standard desktop computers (16Gb of memory). Within pixel-year combinations, we use non-uniform random sampling to overweight specific parts of the predictor space. For inference on the FWI-month interaction, we set different sampling probabilities for FWI values above and below the empirical FWI-quantile at  $p_{\text{FWI}}$  for each pixel-year. Values above the threshold are expected to correspond to more fire-prone conditions, and we over-represent them, e.g., by fixing sampling probabilities  $p_{\text{SS}} = 0.9$  for FWI values below the threshold. To appropriately

identify seasonal effects, we choose the month among June–October at random. For instance, high FWI values tend to be less frequent in October, but uniform subsampling of months gives them more weight. With this scheme, we obtain a positive sampling probability  $p_k > 0$  for each observation  $N_k$  in (4), and likelihood weights are  $\omega_k = 1/p_k$  for the selected observations. Simulation experiments (see Supplement §8.3) motivated taking  $(p_{\text{FWI}}, p_{\text{SS}}) = (0.7, 0.9)$ .

### 3.5 Fully Bayesian inference using INLA-SPDE

Integrated nested Laplace approximation (INLA [Rue et al. 2009](#), [Lindgren & Rue 2015](#), [Opitz 2017](#)) is a Bayesian technique for generalized additive models with Gaussian random effects. It uses astutely designed deterministic approximations for accurate posterior inference on model parameters, random effects and predictions conditional on data. INLA enables transfer of information across components, appropriate uncertainty assessment and estimation of shared effects. We implement Penalized Complexity priors (PC priors, [Simpson et al. 2017](#)) in our models to control the complexity of model components. Such priors penalize the distance of the prior of a model component towards a simpler baseline at a constant rate.

Owing to the large number of pixels in our problem, spatial Gaussian random effects and their conditional distributions must be tractable in this setting. We use the Matérn covariance function for random effects (denoted  $g$ ), given as follows for two points  $s_1$  and  $s_2$ :

$$\text{Cov}\{g(s_1), g(s_2)\} = \sigma^2 2^{1-\nu} (\kappa \|s_1 - s_2\|)^\nu K_\nu(\kappa \|s_1 - s_2\|) / \Gamma(\nu), \quad \sigma, \nu > 0,$$

with Euclidean distance  $\|\cdot\|$ , gamma function  $\Gamma$ , the modified Bessel function of the second kind  $K_\nu$ , and the standard deviation and smoothness parameters  $\sigma$  and  $\nu$ . The empirical range at which the correlation drops to approximately 0.1 is  $r = \sqrt{8\nu}/\kappa$ . Numerically convenient representations through approximating Gauss-Markov random fields (GMRF, characterized by sparse precision, i.e., inverse covariance, matrices) can be constructed by solving a stochastic partial differential equation (SPDE, [Lindgren et al. 2011](#), [Krainski et al. 2018](#)), where we fix the smoothness  $\nu$  at unity. The discretization points are chosen as the nodes of a finite element representation (e.g., the triangulation of space for  $d = 2$ , or spline nodes for  $d = 1$ ), which enables efficient inference for random effects representing spatial variation ( $d = 2$ ) or nonlinear functions ( $d = 1$  for the FWI and FA effects). Our spatial triangulation mesh in [Figure 3](#) has 1114 nodes. It is less dense in the extended zone around the study area to ensure that SPDE boundary conditions have negligible influence on the study area. The four splines knots for FWI and FA are evenly spaced throughout the feature space.

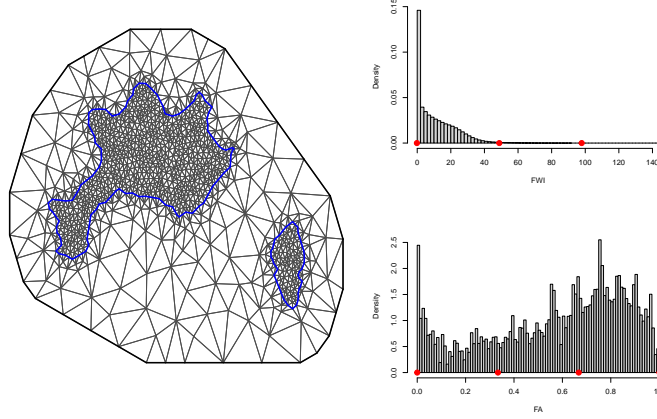


Figure 3: Discretization of random effects with SPDE-based Gaussian prior processes. Left: Triangulation mesh of the study area (blue contours) for the SPDE approach. Neumann boundary conditions are set on the exterior (black) boundary to obtain a unique solution. The finite element solution defines a Gauss–Markov random vector with one variable in each node. Right: Histograms of FWI and FA values. The red points indicate where the spline knots are placed.

## 4 Modeling point processes with moderate and extreme marks

Point processes govern the space-time point patterns of occurrences; size processes govern the moderate-level and extreme quantitative marks. We write  $N_{it}$  for the number of wildfire occurrences on day  $t \in \{1, \dots, n\}$  and over the  $8\text{km} \times 8\text{km}$  grid cell  $i \in \{1, \dots, 1143\}$  with centroid  $s_i$ , and  $\mathcal{A}_{i,t} \subset \mathcal{D}$  for the space-time cell with volume  $|\mathcal{A}_{i,t}| = 64 \text{ (km}^2 \times \text{day)}$ . If  $N_{it} > 0$ , we let  $\mathbf{Y}_{it} = (Y_{it,1}, \dots, Y_{it,N_{it}}) \in (1, \infty)^{N_{it}}$  denote the corresponding quantitative marks. We write  $z_k(s, t)$  ( $k = 1, \dots, K$ ) for known deterministic covariates.

We model data of escaped fires ( $> 1 \text{ ha}$ ), whose occurrence structure is captured by a regression component COX defining a LGCP. A logistic regression component BIN is used to classify fires into moderate (0) and large (1) according to exceedance above a fixed threshold  $u$ . Based on Figure 2, we consider a fire size  $Y_{it,k}$  to be extreme if  $Y_{it,k} > 79\text{ha}$  ( $k = 1, \dots, N_{it}$ ); i.e.,  $u = 79$ . We write  $\mathbf{R}_{it} = (R_{it,1}, \dots, R_{it,N_{it}}) \in \{0, 1\}^{N_{it}}$  for the vector of binary exceedance indicators  $R_{it,k} = \mathbb{I}(Y_{it,k} > u)$ . Moderate wildfire sizes  $Y_{it,k} \in (1, u]$  are modeled through a Beta regression component BET applied to pretransformed values  $(Y_{it,k} - 1)/(u - 1)$ . The Beta distribution, usually parametrized by two shape parameters  $a, b > 0$ , is here parametrized through a precision parameter  $\phi = a + b > 0$  and the mean  $\mu_{it}^{\text{BET}} = a/(a + b) \in (0, 1)$  with logit-link function, such



that  $a = \mu_{it}^{\text{BET}} \phi$  and  $b = \phi(1 - \mu_{it}^{\text{BET}})$ ; it is a flexible location-shape family for interval-valued data, which can be used with INLA. For large wildfires, we build on the extreme-value framework in §3.1 and model excesses  $Y_{it} - u > 0$  above  $u$  through a GPD regression component GPD to characterize extreme wildfires. Following Opitz et al. (2018), we use a log-link function for the median  $\mu_{it}^{\text{GPD}}$  of the GPD.

Some hyperparameters (e.g., precision parameters of priors for fixed effects) are fixed a priori, but those that may strongly influence the posterior model structure are estimated. Priors are fully detailed in the Supplement §8.4.

#### 4.1 Bayesian hierarchical multi-response regression

Our modeling assumptions in §3.3 entail the following structure for the linear COX predictor:

$$\mu_{it}^{\text{COX}} = \log \int_{\mathcal{A}_{it}} \lambda(s, t) d(s, t) = \log \lambda(s_i, t) + \log |\mathcal{A}_{it}|.$$

We construct the system of regression equations in a Bayesian generalized additive mixed model (GAMM) as follows:

$$\begin{aligned} N_{it} \mid \mu_{it}^{\text{COX}} &\sim \text{Poisson}\{\exp(\mu_{it}^{\text{COX}})\}, \\ R_{it,k} \mid \mu_{it}^{\text{BIN}} &\sim \text{Bernoulli}\{\text{logit}^{-1}(\mu_{it}^{\text{BIN}})\}, \quad k = 1, \dots, N_{it}, \\ \{Y_{it,k} - u \mid R_{it,k} = 1, \mu_{it}^{\text{GPD}}\} &\sim \text{GPD}\{\exp(\mu_{it}^{\text{GPD}}), \xi\}, \\ \{(Y_{it,k} - 1)/(u - 1) \mid R_{it,k} = 0, \mu_{it}^{\text{BET}}\} &\sim \text{Beta}\{\text{logit}^{-1}(\mu_{it}^{\text{BET}}), \phi\}; \end{aligned}$$

$$\mu_{it}^{\text{COMP}} = \sum_{k=1}^K g_k^{\text{COMP}} \{z_k(s_i, t); \boldsymbol{\theta}^{\text{COMP}}, \boldsymbol{\theta}^{\text{SHR}}\}, \quad \text{COMP} = \{\text{COX}, \text{BIN}, \text{GPD}, \text{BET}\};$$

$$\boldsymbol{\theta} = (\xi, \phi, \boldsymbol{\theta}^{\text{COX}}, \boldsymbol{\theta}^{\text{BIN}}, \boldsymbol{\theta}^{\text{GPD}}, \boldsymbol{\theta}^{\text{BET}}, \boldsymbol{\theta}^{\text{SHR}}) \sim \text{Hyperpriors},$$

where terms  $g_k^{\text{COMP}}$  capture linear or nonlinear influence of the covariates in the corresponding model component. The specifics of  $\boldsymbol{\theta}$  are discussed below.

By construction, the intensity function  $\lambda_{\text{exc}}$  of the point process of large fires satisfies  $\lambda_{\text{exc}}(s_i, t) \leq \lambda(s_i, t)$ . The exceedance probability  $\text{logit}^{-1} \mu_{it}^{\text{BIN}} = \lambda_{\text{exc}}(s_i, t) / \lambda(s_i, t)$  defines the independent Bernoulli probability of the full point pattern in COX. Since  $\lambda_{\text{exc}}(s_i, t) = \exp(\mu_{it}^{\text{BIN}}) \exp(\mu_{it}^{\text{COX}}) / \{1 + \exp(\mu_{it}^{\text{BIN}})\}$  and typically  $\exp(\mu_{it}^{\text{BIN}}) \approx 0$ , we obtain  $\log \lambda_{\text{exc}}(s_i, t) \approx \mu_{it}^{\text{BIN}} + \mu_{it}^{\text{COX}}$ .

#### 4.2 Sharing latent effects

For maximal flexibility, we could incorporate mutually independent spatial effects into all model components. However, models would become overly complex, with too many spatial effects and hyperparameters to estimate, and with

high posterior uncertainties in the spatial effects of the BIN and GPD components due to the relatively small number of large wildfires. We strike a balance by sharing spatial random effects between model components of the point and size processes, though with a preliminary model selection procedure (see §5.1) that avoids compromising the quality of model fit and predictions. We set SPDE-based spatial GMRF priors  $g^{\text{COX-BET}}$ ,  $g^{\text{COX-BIN}}$  and  $g^{\text{BIN-GPD}}$  (recall §3.5) for the shared spatial effects. We use superscripts to indicate the two components into which we jointly incorporate an effect, and we use  $n$  to indicate the number of latent random variables for the corresponding effect (in superscript):

$$\begin{aligned} g^{\text{COX-BET}}(s_i) &\sim \mathcal{GP}_{2\text{D-SPDE}}(\boldsymbol{\omega}_1), & n^{\text{COX-BET}} &= 1114, \\ g^{\text{COX-BIN}}(s_i) &\sim \mathcal{GP}_{2\text{D-SPDE}}(\boldsymbol{\omega}_2), & n^{\text{COX-BIN}} &= 1114, \\ g^{\text{BIN-GPD}}(s_i) &\sim \mathcal{GP}_{2\text{D-SPDE}}(\boldsymbol{\omega}_3), & n^{\text{BIN-GPD}} &= 1114, \end{aligned}$$

where  $\boldsymbol{\omega}_1$ ,  $\boldsymbol{\omega}_2$  and  $\boldsymbol{\omega}_3$  consist of separate Matérn range  $r$  and standard deviation  $\sigma$  parameters with PC priors (Fuglstad et al. 2018). Each shared effect is additively included in the linear predictor of the second component and then shared towards the first component with a scaling factor  $\beta \in \mathbb{R}$ , with superscripts to denote the two components. We denote the vector of sharing-related hyperparameters by  $\boldsymbol{\theta}^{\text{SHR}} = (\boldsymbol{\omega}_1, \boldsymbol{\omega}_2, \boldsymbol{\omega}_3, \beta^{\text{COX-BET}}, \beta^{\text{COX-BIN}}, \beta^{\text{BIN-GPD}})$ , and use flat, independent zero-centered Gaussian hyperpriors for the scaling factors.

Sharing allows modeling of residual spatial effect components that jointly affect multiple model responses, such as land-use features at the Wildland-to-Urban interface (Stewart et al. 2007), where human activities intermingle with wildland vegetation. Accurate sharing improves parsimony of the model and borrows estimation strength for random effects across model components by simultaneously using data from several response types. Expert knowledge may guide the choice of shared spatial effects. Sharing can provide novel scientific insights into the interplay of occurrences and sizes for moderate and large wildfires among spatial zones.

### 4.3 Prior structure of linear predictors

We let  $z_{\text{FWI}}(s_i, t)$  and  $z_{\text{FA}}(s_i, t)$  denote the average FWI and FA on day  $t$  in grid cell  $i$ , and by  $a(t)$  and  $m(t)$  the corresponding year and month of day  $t$ . Using notation  $\alpha$  for the intercept and  $g$  for the other GAMM components, the prior structure of the model component COX for escaped fire occurrences is

$$\begin{aligned} \mu_{it}^{\text{COX}} = & \alpha^{\text{COX}} + g_1^{\text{COX}}(s_i) + \beta^{\text{COX-BET}} g^{\text{COX-BET}}(s_i) + \beta^{\text{COX-BIN}} g^{\text{COX-BIN}}(s_i) \\ & + g_2^{\text{COX}}\{z_{\text{FA}}(s_i, t)\} + g_3^{\text{COX}}\{z_{\text{FWI}}(s_i, t); m(t)\} \\ & + g_4^{\text{COX}}\{a(t)\} + g_5^{\text{COX}}\{m(t)\}; \end{aligned}$$

$$\begin{aligned}
g_1^{\text{COX}}(s_i) &\stackrel{\text{iid}}{\sim} \mathcal{N}\{0, 1/\tau_1\}, & n_1^{\text{COX}} &= 1143, \\
g_2^{\text{COX}}(\bullet) &\sim \mathcal{GP}_{\text{1D-SPDE}}(\phi_1), & n_2^{\text{COX}} &= 4, \\
g_3^{\text{COX}}(\bullet; m) &\sim \mathcal{GP}_{\text{1D-SPDE}}(\phi_2), \\
g_3^{\text{COX}}(z_{\text{FWI}}; \bullet) &\sim \mathcal{GP}_{\text{RW1}}(1/\tau_2), & n_3^{\text{COX}} &= 4 \times 5 = 20, \\
g_4^{\text{COX}}(\bullet) &\sim \mathcal{GP}_{\text{RW1}}(1/\tau_3), & n_4^{\text{COX}} &= 20, \\
g_5^{\text{COX}}(\bullet) &\sim \mathcal{GP}_{\text{RW1}}(1/\tau_4), & n_5^{\text{COX}} &= 5;
\end{aligned}$$

$$\theta^{\text{COX}} = \{\alpha^{\text{COX}}, \phi_1, \phi_2, \tau_1, \tau_2, \tau_3, \tau_4\} \sim \text{Hyperpriors}.$$

Spatial occurrence hot-spots (see Supplement §8.1), may arise due to time-invariant land-use features. Moreover, spatial variation may be shared from patterns in the BET and BIN components through the components  $g^{\text{COX-BET}}(s_i)$  and  $g^{\text{COX-BIN}}(s_i)$ , respectively. The month and year effects,  $g_4^{\text{COX}}$  and  $g_5^{\text{COX}}$ , capture spatially homogeneous temporal variations in occurrence intensities. They are endowed with first-order random-walk priors  $\mathcal{GP}_{\text{RW1}}$  with a sum-to-zero constraint for identifiability; e.g., for the yearly effect and for  $a = 1995, \dots, 2013$ ,

$$g_4^{\text{COX}}(a+1) - g_4^{\text{COX}}(a) \sim \mathcal{N}(0, 1/\tau_3), \quad \sum_{i=1995}^{2014} g_4^{\text{COX}}(i) = 0.$$

The quadratic B-spline functions of FWI and FA are endowed with priors  $\mathcal{GP}_{\text{1D-SPDE}}$ , constrained to zero at the left boundary 0 and constrained to sum to zero, respectively. Most wildfires in the region are caused by human activity, possibly leading to a nonlinear relationship between FA and occurrence intensity, as dense forest areas are often exposed to low human activity. We allow for monthly variation of the nonlinear FWI effect through separate  $\mathcal{GP}_{\text{1D-SPDE}}$ -terms in  $g_3$  for each month, linked across successive months with a  $\mathcal{GP}_{\text{RW1}}$ -structure in the prior model.

The regression equation used for the Bernoulli process is

$$\begin{aligned}
\mu_{it}^{\text{BIN}} &= \alpha^{\text{BIN}} + g^{\text{COX-BIN}}(s_i) + \beta^{\text{BIN-GPD}} g^{\text{BIN-GPD}}(s_i) + g_1^{\text{BIN}}\{z_{\text{FWI}}(s_i, t)\} \\
&\quad + g_2^{\text{BIN}}\{z_{\text{FA}}(s_i, t)\} + g_3^{\text{BIN}}\{a(t)\};
\end{aligned}$$

$$\begin{aligned}
g_k^{\text{BIN}}(\bullet) &\sim \mathcal{GP}_{\text{1D-SPDE}}(\zeta_k), \quad k = 1, 2, & n_1^{\text{BIN}}, n_2^{\text{BIN}} &= 5, \\
g_3^{\text{BIN}}(\bullet) &\sim \mathcal{GP}_{\text{RW1}}(1/\tau_5), & n_3^{\text{BIN}} &= 5;
\end{aligned}$$

$$\theta^{\text{BIN}} = \{\alpha^{\text{BIN}}, \zeta_1, \zeta_2, \tau_5\} \sim \text{Hyperpriors}.$$

The linear predictor of the Bernoulli probability has a simpler form than that of the occurrence component but still allows the capture of specific nonlinear effects of FWI and FA. In Figure 1, we discern hot-spot areas of large fire occurrences

that differ substantially from the overall occurrence structure, and we aim to capture these residual effects through the shared spatial effects.

The prior structure for the two mixture components of quantitative marks is

$$\begin{aligned}\mu_{it}^{\text{BET}} &= \alpha^{\text{BET}} + g^{\text{COX-BET}}(s_i) + g_1^{\text{BET}}\{z_{\text{FWI}}(s_i, t)\} + g_2^{\text{BET}}\{z_{\text{FA}}(s_i, t)\}, \\ \mu_{it}^{\text{GPD}} &= \alpha^{\text{GPD}} + g^{\text{BIN-GPD}}(s_i) + g_1^{\text{GPD}}\{z_{\text{FWI}}(s_i, t)\} + g_2^{\text{GPD}}\{z_{\text{FA}}(s_i, t)\} \\ &\quad + g_3^{\text{GPD}}\{a(t)\};\end{aligned}$$

$$\begin{aligned}g_k^{\text{BET}}(\cdot), g_k^{\text{GPD}}(\cdot) &\sim \mathcal{GP}_{\text{1D-SPDE}}(\kappa_k), \quad k = 1, 2, \quad n_1^{\text{GPD}}, n_2^{\text{GPD}}, n_1^{\text{BET}}, n_2^{\text{BET}} = 5, \\ g_3^{\text{GPD}}(\cdot) &\sim \mathcal{GP}_{\text{RW1}}(1/\tau_6), \quad n_3^{\text{GPD}} = 5;\end{aligned}$$

$$\theta^{\text{MARK}} = \{\alpha^{\text{GPD}}, \alpha^{\text{BET}}, \kappa_1, \kappa_2, \tau_6\} \sim \text{Hyperpriors}.$$

A year effect, endowed with a random-walk prior, was included in some of the components (COX, BIN, GPD) since [Pimont et al. \(2021\)](#) find that FWI and FA alone cannot capture yearly variation in very large fires, especially for the year 2003. In all components (BET, BIN, COX, GPD), we allow for non-linear relationships with respect to FWI or FA.

#### 4.4 Alternative model specifications

We also consider size processes that do not model the moderate-level and extreme marks separately; i.e., with no mixture representation of the size process. We use either the Gamma distribution for the full range of marks:  $Y_{it,k} \mid \mu_{it}^{\text{SIZE}} \sim \text{Gam}\{\exp(\mu_{it}^{\text{SIZE}}), \phi_{\text{Gam}}\}$ , or the Normal distribution for the logarithmic transformed marks:  $\log Y_{it,k} \mid \mu_{it}^{\text{SIZE}} \sim \mathcal{N}\{\exp(\mu_{it}^{\text{SIZE}}), \phi_{\mathcal{N}}\}$ , where the distributions are parameterized by the link function  $\mu_{it}^{\text{SIZE}}$  modeling the mean and precision parameters  $\phi_{\text{Gam}} = \exp(\mu_{it}^{\text{SIZE}})^2 / \text{Var}(Y_{it,k})$  and  $\phi_{\mathcal{N}} = 1 / \text{Var}(\log Y_{it,k})$ , respectively. In both cases

$$\begin{aligned}\mu_{it}^{\text{SIZE}} &= \alpha^{\text{SIZE}} + g^{\text{SIZE-COX}}(s_i) + g_1^{\text{SIZE}}\{z_{\text{FWI}}(s_i, t)\} + g_2^{\text{SIZE}}\{z_{\text{FA}}(s_i, t)\} \\ &\quad + g_3^{\text{SIZE}}\{a(t)\} + g^{\text{SIZE}}(s_i);\end{aligned}$$

$$\begin{aligned}g_k^{\text{SIZE}}(\cdot) &\sim \mathcal{GP}_{\text{1D-SPDE}}(\boldsymbol{\iota}_k), \quad k = 1, 2, \quad n_1^{\text{SIZE}}, n_2^{\text{SIZE}} = 5, \\ g_3^{\text{SIZE}}(\cdot) &\sim \mathcal{GP}_{\text{RW1}}(1/\tau_7), \quad n_3^{\text{SIZE}} = 5;\end{aligned}$$

$$\theta^{\text{SIZE}} = \{\alpha^{\text{SIZE}}, \boldsymbol{\iota}_1, \boldsymbol{\iota}_2, \tau_7\} \sim \text{Hyperpriors},$$

where the spatial effects  $g^{\text{SIZE-COX}}(s_i)$  and  $g^{\text{SIZE}}(s_i)$  are controlled by Matérn parameters  $\omega_4$  and  $\omega_5$ , similar to those in §4.2.

## 5 Results

### 5.1 Model selection and comparison

Estimation was carried out using the INLA-SPDE approach described in §3.5 by applying the subsampling scheme proposed in §3.4.

In a preliminary analysis of the regression models described in §4, we used the Widely Applicable Information Criterion (WAIC, [Watanabe 2010](#)) in a step-wise manner to compare nested models with different components in the regression equations (e.g., linear vs nonlinear effects of explanatory variables) to choose their final forms. Due to the small number of extreme wildfires, their influence on WAIC is relatively small; we thus subsequently proceed with other model comparison tools that give more weight to large wildfires and their prediction.

We label the model with prior structure detailed in §4.3 M1, the model without spatial effects in the size and extreme occurrence components M2, and the model M2 but without monthly variation in the FWI effect M3. The latter is most similar to the best-performing model described in [Pimont et al. \(2021\)](#) but performs slightly better (not shown) for the performance metrics used in that paper.

We also use other models from the wildfire modeling literature. We let M4 and M5 denote the models with the same point process model as M1 but with no mixture representation of the size process, for which we use a log-Normal or a Gamma response distribution with prior structure detailed in §4.4, respectively. These models do not differentiate between extreme and non-extreme fires, but the two response distributions have been found to be good modeling candidates in [Joseph et al. \(2019\)](#), though they do not include shared random effects.

For the observed individual fires in the training (1995–2014) and validation (2015–2018) periods, we generated posterior predictive distributions of each model based on 500 posterior simulations. First, we evaluated the models’ ability to predict exceedances above increasingly high severity thresholds of burnt area of individual fires (given by the empirical 90/99% quantiles) using the AUC ([Fawcett 2006](#)) and the Brier score ([Brier 1950](#)). Second, we used the continuous ranked probability score (CRPS) ([Matheson & Winkler 1976](#)) to compare simulated predictive distributions of burnt areas. We also considered the threshold-weighted CRPS (twCRPS) ([Gneiting & Ranjan 2011](#)), with weight given by the indicator  $\mathbb{1}_{y \geq 100\text{ha}}$ , in order to disregard prediction performance below 100 ha. We also computed the scaled CRPS (sCRPS) suggested by [Bolin & Wallin \(2020\)](#) for averages of CRPS over non-identical predictive distributions. For these analyses, we keep the original locations of observed fires, and simulation is done from the size components only.

By combining posterior simulations of the occurrence and size components, we also evaluated predictive performance for burnt areas aggregated at different temporal and spatial scales, using the sCRPS: départements vs. whole region; yearly vs. monthly.

Table 1 shows good relative performance of M1 for all scores when evaluating wildfire predictions on the validation set. To better grasp the uncertainty in

	Score	Model				
		M1	M2	M3	M4	M5
Individual fires, $n = 823$	sCRPS	2.74	2.87	2.94	2.84	3.19
	p-value	-	< 5%	< 1%	< 5%	< 5%
	CRPS	28.48	28.48	28.59	29.36	29.78
	p-value	-	50%	24%	< 1%	< 1%
	twCRPS	20.11	20.03	20.12	20.26	20.59
	p-value	-	74%	46%	18%	7%
	Brier <sub>q90</sub>	0.0855	0.0868	0.0866	0.0944	0.0967
	p-value	-	< 5%	6%	< 1%	< 1%
	Brier <sub>q99</sub>	0.0106	0.0105	0.0106	0.0107	0.0107
	p-value	-	85%	64%	22%	35%
	1 - AUC <sub>q90</sub>	0.3052	0.3502	0.3516	0.3184	0.3122
	p-value	-	< 5%	< 5%	40%	41%
Dép-overall, $n = 15$	1 - AUC <sub>q99</sub>	0.0949	0.2001	0.1515	0.2612	0.3795
	p-value	-	11%	25%	< 5%	< 5%
Dép-month, $n = 75$	sCRPS	4.43	4.41	4.41	4.45	4.62
	p-value	-	58%	57%	48%	19%
	sCRPS	3.55	3.62	3.64	3.62	3.58
	p-value	-	7%	7%	9%	39%

Table 1: sCRPS, CRPS, twCRPS, Brier and AUC scores for individual fires and two different spatiotemporal aggregations (averaged over  $n$  observations), based on 500 simulations of posterior models on the validation set. A lower score is better.

scores, we show p-values of a permutation test assessing the significance of negative values in the differences of scores between M1 and the other models, based on 2000 permutations. For the sCRPS, the seemingly small score differences are all significant at the 5% level. A general finding is that the extra complexity of model M1 compared to competitor models does not hamper prediction. Using sophisticated structures such as the mixture representation of size processes, sharing and monthly variation of FWI effect tends to improve prediction; it further allows for novel scientific insights presented in §6.

Comparison of M1 and M2 confirms the benefits of incorporating spatial random effects in the size model components in M1 using parsimonious structures, thanks to the sharing detailed in §4.2. M1 generally performs better than M2, though in some cases improved scores have relatively low confidence levels in light of the p-values. Performances of M2 and M3 are similar for predicting wildfire sizes and their aggregation. Model M1 performs better than M4 and M5 especially with Brier and AUC scores for the occurrence of extreme events in the validation set. Despite good scores of M5 on the training set (not shown), its comparatively worse results on the validation sample suggest that the Gamma distribution for burnt areas does not predict the extremes in new data well. Similar behavior arises for the model M4 with log-Normal fire sizes. Mixture modeling of the tail and the body of wildfire sizes generally performs better.

Since empirical means of CRPS values may be unstable with heavy-tailed data, we also visually compare the full empirical CRPS distribution between models (see Supplement §8.5). Model M1 has better scores than M4 and M5, with lower values especially in the upper CRPS tail, while the case against M2 is less clear.

## 5.2 Visual inspection of posterior predictive densities

We also assess the predictive behavior of our chosen model M1 with visual diagnostics, especially for tail behavior. First, we assess whether the size component correctly predicts extreme wildfires at the regional level of specific départements. In Figure 4, we use simulations from the posterior model at pixel-days where fires have been observed to compare empirical and predicted excess probabilities over increasingly high thresholds, starting at 100ha. Predictions are generally good since most empirical exceedance probabilities fall within the inter-quantile range of simulations, except for the départements of Var and Haute-Corse with small underestimation at very large thresholds. These two départements have large continuous forest areas and saw unusually many large wildfires in the summer of 2017. Much of their land has acidic soils that favor biomass production and are covered by tall and dense shrubland, so 2017 fires were harder to contain due to their higher heat release. Overall, the tail behavior in fire-prone and less fire-prone regions is well discriminated by the model.

Next, we consider the occurrence component by comparing the number of simulated and observed fires aggregated by year over the study region (Figure 5, left display). Observed annual fire numbers for both test and training set fall within the inter-quantile range of simulations for more than half of the study period. M1 captures the relatively high observed numbers of 2001, 2003 and 1998 (training) and 2017 (test), while it also accurately predicts the sharp decrease in 2018.

Lastly, we jointly evaluate the size and occurrence components of our model M1. We aggregated simulated burnt areas by year, over the whole spatial region in Figure 5 (right display), and over départements in Figure 6. The global time trend in observed burnt areas is well captured throughout the years in Figure 5, with inter-quantile coverage of 42%. M1 captures the exceptional peak in 2003, which is poorly predicted by M4 and M5 and the Firelihood model of Pimont et al. (2021). M1 also succeeds in accurately predicting the moderately high burnt areas in 2001 and 2017, and it generally discriminates well between fire conditions leading to small, moderate, large and very large fire numbers. Figure 6 further shows that regional differences across départements are well captured by M1, with most panels showing roughly 50% inter-quantile range coverage. Overall, our model appropriately captures spatiotemporal variation and provides satisfactory regionalized forecasts for operational purposes.

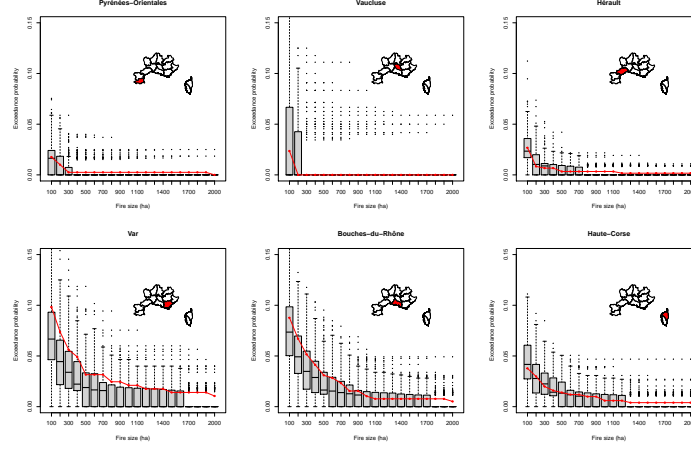


Figure 4: Exceedance probability plots for six départements (in red on the maps) in the validation set (2015–2018). Boxplots are based on 200 posterior simulations. Red lines represent observed empirical exceedance probabilities.

## 5.3 Principal results of the main model M1

### 5.3.1 Covariate effects

For the COX component, Figure 7 shows the month-specific FWI effect, with significant differences across months. For easier comparison, we have subtracted the same value from all curves such that the posterior mean is 0 for FWI= 0 in September. Throughout, the posterior means are monotonically increasing up to FWI of 75. Curves flatten for higher values of FWI especially at the beginning and end of the wildfire season, with a slight decrease of the curve towards the highest FWI.

The posterior partial effect of FA on the COX component in Figure 8 indicates a “bump”-shaped effect of FA, which is significant based on pointwise credible intervals. Very high FA can be considered as a good proxy for relatively few human-induced wildfire ignitions, while very low FA means lack of fuel. Clearly, expected wildfire ignition numbers are not proportional to forest area.

As to temporal partial effects without spatial variation (Figure 8), the posterior year effect suggests a strong, significant drop in wildfire activity after 2003, potentially related to policy changes after the exceptional 2003 events. The partial month effect (right display of Figure 8, corresponding to the intercept of its combined effect with FWI in Figure 7) is lowest at the start of the wildfire season and peaks in August.

As to the probability of occurrence of large fires (BIN), Figure 9 (middle display) highlights a strong positive posterior effect of FWI, increasing monotonically and significantly up to FWI values of around 75, before it dampens



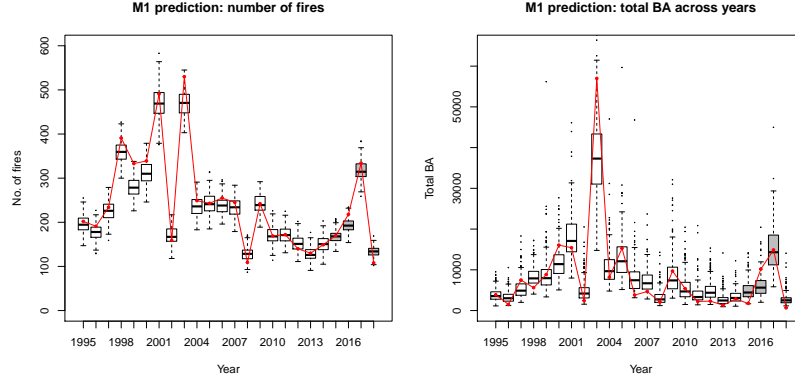


Figure 5: Boxplots by year for the predicted number of fires (left) and predicted total burnt area (right) across the whole region from 200 simulations of the posterior model. The grey boxplots indicate the out-sample years. The red lines represent the observed annual total number of fires and total burnt area in the whole region.

at very large FWI values, similar to the COX component: large wildfires are relatively more frequent with moderate to high FWI values. The probability of large wildfires tends to increase with increasing FA in a grid cell (Figure 9, left display), which is reasonable since larger FA fuel is available over large areas. The pointwise credible bounds of yearly effects across the study period suggest that the occurrence of large events was significantly higher around the peak in 2003.

In the additive effects of the two mixture components GPD and BET of the size distribution shown in Figures 10 we find similar posterior effects of FWI and forest area for extreme and moderate sizes. Posterior estimates imply that fires become larger when FWI increases up to around 60 but the effect flattens for higher FWI. Increasing FA leads to increasing wildfire size in both components up to 50% and then reaches a plateau. For the year effect in the extreme component GPD, no clear trend arises, though 2003 has a significantly higher effect than 1998.

### 5.3.2 Sharing effects induce correlated wildfire activity components

We here focus only on the spatial effects that were shared between model components. The 95% credible intervals for the scaling parameters  $\beta^{\text{COX-BETA}}$ ,  $\beta^{\text{COX-BIN}}$  and  $\beta^{\text{BIN-GPD}}$  do not cover 0; their posterior estimates for the triplet (2.5% quantile, mean, 97.5% quantile) are (6.4, 10.3, 14.0), (−3.1, −1.8, −0.9), and (0.5, 1.0, 1.6), respectively. The posterior mean of  $\beta^{\text{COX-BETA}}$  is positive and the one of  $\beta^{\text{COX-BIN}}$  is negative, which confirms significant positive and negative sharing between the COX and BETA, and the COX and BIN model

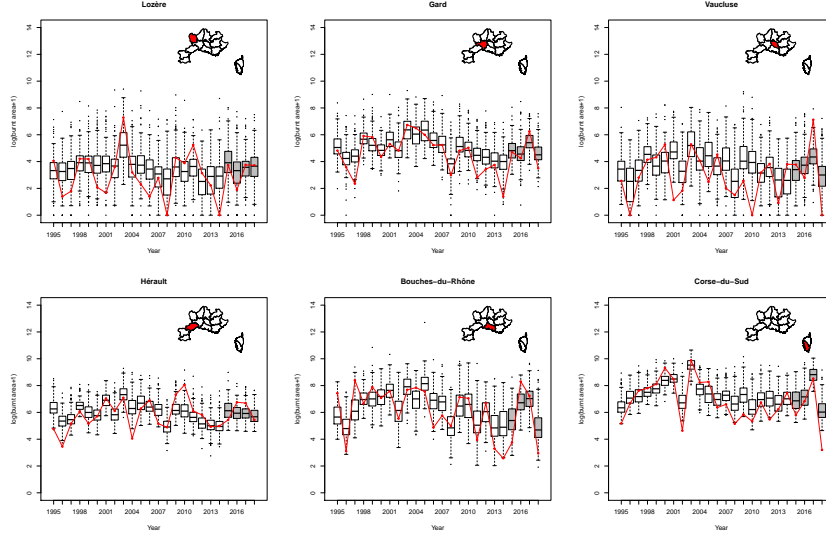


Figure 6: Boxplots by year and département for the predicted logarithmic total burnt area from 200 simulations of the model. Red dots represent the observed annual log total burnt area in each département. The département used for each panel is shown in red on the maps.

components, respectively; these findings provide new spatial insights for fire risk management in §6. The posterior means for the effective range parameters of the shared spatial fields,  $r^{\text{COX-BETA}}$ ,  $r^{\text{COX-BIN}}$  and  $r^{\text{BIN-GPD}}$ , are 34.3km, 26.2km and 156.9km, respectively. Posterior mean maps of their corresponding spatial random effects are shown in the Supplement §8.6.

Sharing indeed decreases uncertainty by borrowing estimation strength between model components. The average lengths of 95% posterior credible intervals of variables constituting the random effect shrink by up to 30% (Figure 11) because of a higher observation-to-parameter ratio that makes spatial signals become easier to discern.

To identify the hot-spot regions of spatial random effects, we study credible sets for excursion regions (Bolin & Lindgren 2015). We evaluate where the fields exceed or fall below the thresholds  $u = 0.1$  and  $-u$ , respectively. These thresholds approximately correspond to a 10% increase and decrease, respectively, on the scale of the response when taking into account the log or logistic link. The  $u$ -excursion set with probability  $\alpha$ ,  $E_{u,\alpha}^+(X)$ , is defined as the largest set for which the level  $u$  is exceeded at all locations in the set with probability  $1 - \alpha$ . The negative  $u$  excursion set with probability  $\alpha$ ,  $E_{u,\alpha}^-(X)$ , is defined as the largest set for which the process remains below the level  $-u$  at all locations in the set with probability  $1 - \alpha$ . This approach determines the largest set contained in the exceedance set with a minimum probability threshold, and it assumes a parametric family for the exceedance sets. To visualize excursion

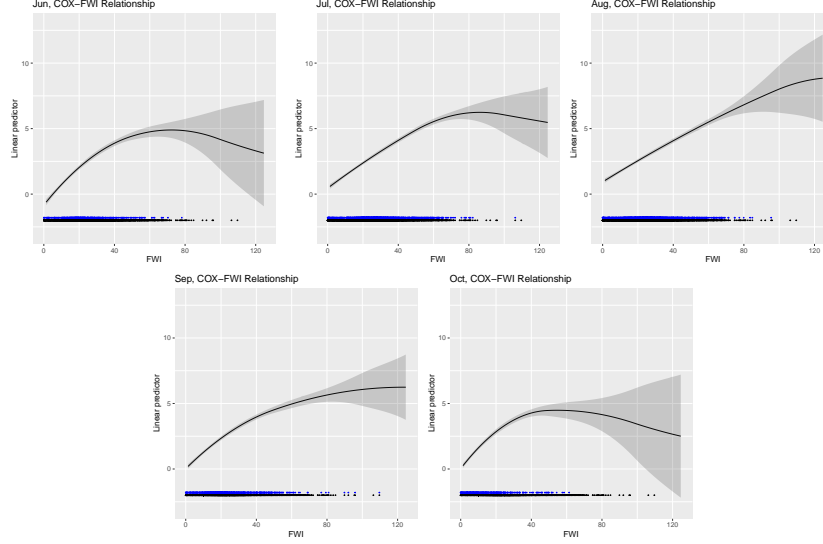


Figure 7: Posterior estimates of  $g_3^{\text{COX}}(\cdot; m) + g_5^{\text{COX}}(m)$ ,  $m = 1, \dots, 5$ , the joint FWI-month effect, for June–October in the linear predictor of the point process (COX) component. The blanket of black and blue points at the bottom of each plot shows FWI values for pixel-days with fires in any month and the specific month, respectively.

sets simultaneously for all values of  $\alpha$ , [Bolin & Lindgren \(2015\)](#) introduced the positive and negative excursion functions  $F_u^+(s) = 1 - \inf\{\alpha \mid s \in E_{u,\alpha}^+\} \in [0, 1]$  and  $F_u^-(s) = 1 - \inf\{\alpha \mid s \in E_{u,\alpha}^-\} \in [0, 1]$ . [Figure 12](#) highlights several hot-spot regions for the shared spatial effects, which we interpret with respect to wildfire management in [§6](#).

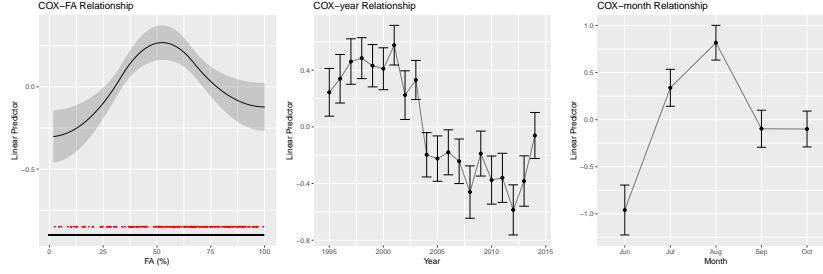


Figure 8: Posterior estimates of  $g_2^{\text{COX}}(\cdot)$  (FA effect, left panel),  $g_4^{\text{COX}}(\cdot)$  (year effect, middle panel) and  $g_5^{\text{COX}}(\cdot)$  (month effect, right panel) in the linear predictor of the point process (COX) component. At the bottom of the left display, the blanket of black and red points shows FA values for pixel-days with moderate and large fires, respectively.

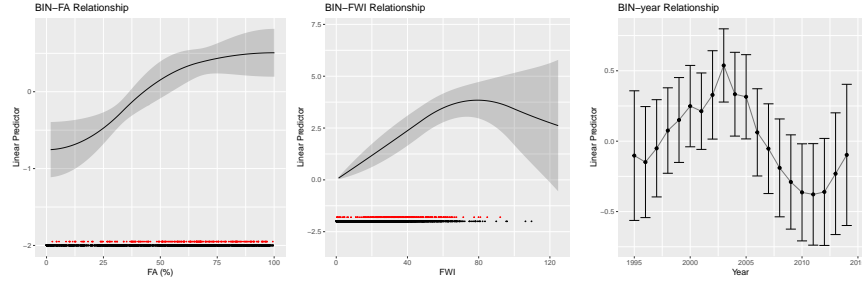


Figure 9: Panels as in Figure 8 but for posterior estimates of  $g_2^{\text{BIN}}(\cdot)$  (FA effect, left panel),  $g_1^{\text{BIN}}(\cdot)$  (FWI effect, middle panel) and  $g_3^{\text{BIN}}(\cdot)$  (year effect, right panel) in the linear predictor of the large wildfire probability component (BIN).

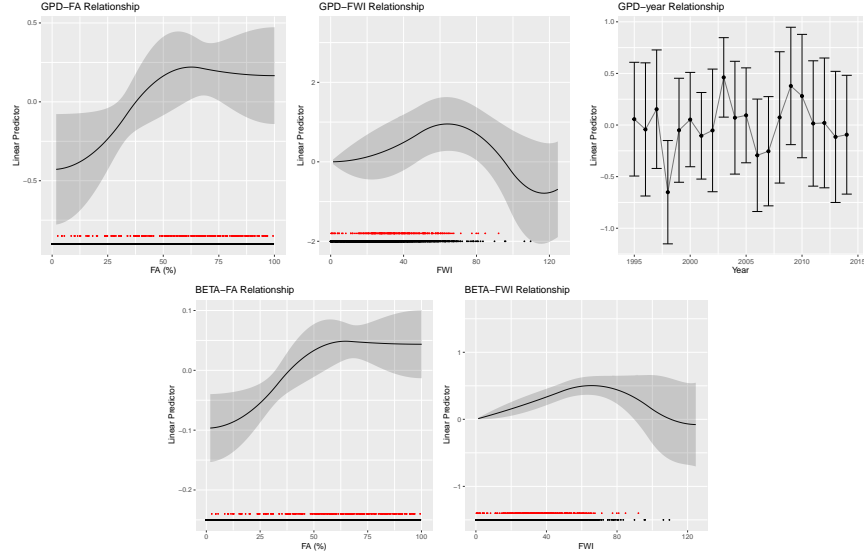


Figure 10: Panels as in Figure 8. Top panels: posterior estimates of  $g_2^{\text{GPD}}(\cdot)$  (FA effect, left),  $g_1^{\text{GPD}}(\cdot)$  (FWI effect, middle) and  $g_3^{\text{GPD}}(\cdot)$  (year effect, right) in the linear predictor of the large wildfire size component (GPD). Bottom panels: posterior estimates of  $g_2^{\text{BETA}}(\cdot)$  (FA effect, left) and  $g_1^{\text{BETA}}(\cdot)$  (FWI effect, right) in the linear predictor of the moderate wildfire size component (BET).

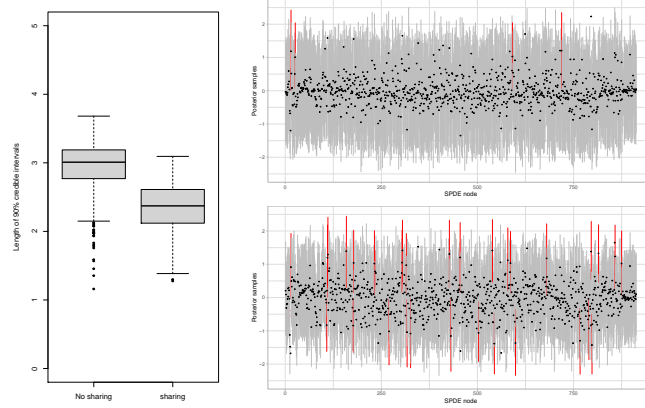


Figure 11: Lengths of the 95% credible intervals of spatial random effect variables at the SPDE triangulation nodes within the study area in the BIN component, based on 500 posterior simulations. Boxplots (left), and error bar plots for the models without (top right) and with sharing (bottom right). Red error bars indicate nodes where the intervals do not include zero.

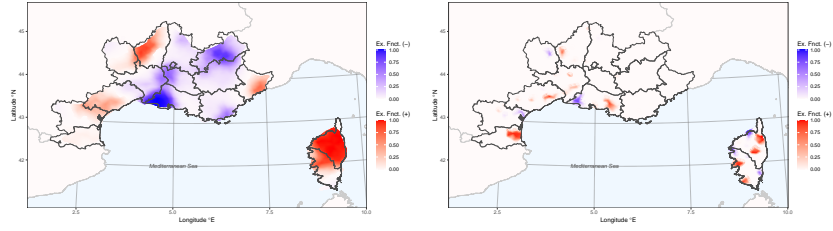


Figure 12: Excursion functions of posterior latent fields above 0.1 and below  $-0.1$ . Plots show  $\max\{F_{0.1}^+(\bullet), F_{0.1}^-(\bullet)\}$  for the shared spatial random fields  $g^{\text{COX-BET}}$  (left panel) and  $g^{\text{COX-BIN}}$  (right panel).

## 6 New insights for wildfire science

### 6.1 FWI and seasonal effects

The estimated FWI effect on all wildfire components (COX, BIN, BET, GPD) is nonlinear with a strong increase when moving from  $\text{FWI} = 0$  towards  $\text{FWI} \approx 60$ – $80$ , followed by a dampening and a slight decrease for extreme FWI values but with relatively wide credible bounds. Moreover, seasonal patterns emerge in the joint FWI-month effect in the occurrence component COX. The common practice of using FWI directly as a proxy for wildfire activity, without a nonlinear transfer function as estimated here, would predict extreme wildfires badly and miss seasonally varying response of fire activity to this index.

A non-linear, even decreasing, response to high FWI and seasonal biases was pointed out in [Pimont et al. \(2021\)](#), and is attributed to the excessively sharp exponential response of FWI to wind speed in its upper range and to the limited ability of the Drought Code (a subcomponent of the FWI) to reproduce live fuel moisture dynamics ([Ruffault et al. 2018](#)). In spring, vegetation budburst produces new foliage with a high water content that is maintained until the onset of the summer drought, typically in early July. The timing of periodic events in plant life cycles (i.e., plant phenology) and stomatal control under drought might also explain why dynamics of soil and vegetation water contents are unsynchronized at certain times. In the new COX model, we allow not only for a seasonal effect but also for different responses of FWI across the five months. The shapes of these monthly responses vary greatly, so seasonal variations cannot be handled solely through a separate seasonal random effect. The response in August did not exhibit any saturation in the upper part of the FWI range, suggesting that higher values in mostly dry conditions correspond to increased fire activity; the contribution of wind to FWI could be adequate in these already-dry conditions. On the contrary, a flattening and notable decrease of the COX response to FWI was observed at  $\text{FWI} \approx 45$ – $50$  for relatively moist conditions in June and October. This supports the hypotheses that the desynchronization of soil and fuel moistures caused by plant phenology in Spring could be involved, and the response of the FWI to high wind would be inaccurate in such moist conditions. July and September, with their mixture of dry and moist days, show intermediate response levels to very high FWI. These findings confirm a need for better wildfire danger indices in the study region.

### 6.2 Time trends during the study period

The year 2003 was catastrophic in terms of fire sizes and burnt area. It has a pivotal role with a decrease of occurrence numbers and sizes afterwards, as captured by the components of our posterior model. In 2003, a heat wave coincided with severe drought conditions, leading to an unusually high number of escaped fires ( $> 1\text{ha}$ ), and of fires larger than  $10\text{ha}$  for several weeks, whose occurrence was not matched by very high values of FWI due to its weaknesses outlined in [§6.1](#). Official policy measures have slightly evolved after 2003, and the aware-

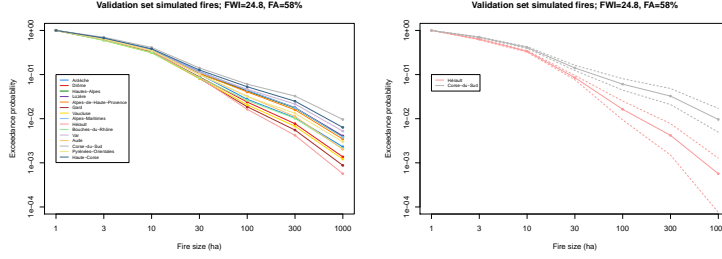


Figure 13: Left: Exceedance probability plots by département from 1000 posterior samples of the model M1 on the validation set given fixed FWI and FA. Right: Same as the left panel, but only for two départements with corresponding 95% credible intervals.

ness of fire managers may also have been raised to strengthen prevention or suppression policies (Pimont et al. 2021).

A finding of our model that should garner attention of operational services is the yearly effect of its BIN component, as the probability of observing a large fire tends to increase over the most years following a decade of continuous decrease. Similar to Evin et al. (2018), no clear time trend was observed for the probability of extreme fires (GPD).

### 6.3 Shared spatial effects for improved regionalized predictions

The shared spatial effects shown in §5.3 highlight regional differences in fire size distributions and allow quantitative interpretations of effects that confirm current understanding of fire risk. They also reveal regional variation in proportions of moderate and extreme fires. In particular, the sharing effect with significantly negative  $\beta^{\text{COX-BIN}}$  can be attributed to different wildland-to-urban interactions. The lowland area in the western Pyrénées-Orientales region, fairly densely populated with a large proportion of abandoned agricultural land intermixed with urban surfaces, appears to have high occurrence intensities, but its combustible area is strongly fragmented so wildfires are mostly small. More fires than expected from weather/climate and forest area occur in densely populated landscapes or in rural landscapes with significant human activities promoting fire ignitions, while landscape fragmentation and landscape management reduce the likelihood of large fires. The COX-BETA sharing effect is highly positive in Corsica, where escaped fires become larger moderate fires more often than elsewhere, perhaps due to longer arrival times of firefighters in remote Corsican forests and by less frequent airborne firefighting. Moreover, extreme fires tend to be more frequent than elsewhere because of large contiguous forests.

Regional disparities in predictions are further illustrated in Figure 13, where the right panel highlights significant differences in probabilities of fires exceeding



increasing thresholds for two regions.

## 7 Conclusion

We have implemented a novel Bayesian spatiotemporal model for wildfire activity with specific components for extreme events, and with shared random effects to account for dependence not explained by covariates. Sharing strategies respond to different considerations. If statistical stability is the focus, then sharing from well-identified model components towards those less informed by data is sensible. If focus is on accurate inference of a specific component (e.g., extremes), then it is sensible to share effects from this component towards others. In both cases, component-specific effects without sharing remain important and should be included as far as data allow estimating them. While our models with sharing did not substantially improve prediction for French wildfires they provide valuable interpretation. In some applications, it may be the only sensible way to incorporate spatial effects in certain response variables. For example, had we chosen a threshold larger than 79ha for large wildfires, we would have had even fewer observations available for the extreme fire size component. A separate spatial effect in this component would provide very wide credible intervals of little practical use.

Our findings improve decision support in wildfire management: shared spatial effects explain how wildfire numbers and extreme sizes interact, with significant disparities between regions; FWI maps must be interpreted with care because of nonlinear and seasonal effect on wildfire risk. Our framework allows for exploring more general space-varying temporal trends in fire weather relationship in future work.

Our approach could provide new insights and improved extreme-value predictions for a variety of other problems. Landslide inventories can be represented as magnitude-marked point processes (Lombardo et al. 2018, 2020, Opitz, Bakka, Huser & Lombardo 2020) with heavy-tailed magnitudes (Stark & Hovius 2001). Another promising application consists in modeling locations, times and values of high-impact events extracted from processes indexed over continuous space and time, such as local extremes in gridded climate data. This would yield a parsimonious representation of extreme events in such processes. While our focus here is on generative and predictive modeling, the adaptation of descriptive tools from stochastic geometry (K-functions, mark correlation functions, see Chiu et al. 2013) would further improve the analysis of point processes with extreme marks. Models for preferentially sampled spatial data (Diggle et al. 2010) can be viewed as marked point processes with shared effects, such that our approach would allow for capturing preferential sampling effects specifically in extreme values.

## Acknowledgement

We would like to thank Anthony Davison for helpful comments and discussions, and the Swiss National Science Foundation for financial support.

## References

- Baddeley, A., Berman, M., Fisher, N. I., Hardegen, A., Milne, R. K., Schumacher, D., Shah, R. & Turner, R. (2010), ‘Spatial logistic regression and change-of-support in Poisson point processes’, Electronic Journal of Statistics **4**, 1151–1201.
- Baddeley, A., Coeurjolly, J.-F., Rubak, E. & Waagepetersen, R. (2014), ‘Logistic regression for spatial Gibbs point processes’, Biometrika **101**(2), 377–392.
- Baddeley, A., Rubak, E. & Turner, R. (2015), Spatial Point Patterns: Methodology and Applications with R, Chapman and Hall/CRC Press.
- Baddeley, A. & Turner, R. (2000), ‘Practical maximum pseudolikelihood for spatial point patterns’, Australian & New Zealand Journal of Statistics **42**(3), 283–322.
- Berman, M. & Turner, T. R. (1992), ‘Approximating point process likelihoods with GLIM’, Journal of the Royal Statistical Society: Series C (Applied Statistics) **41**(1), 31–38.
- Bolin, D. & Lindgren, F. (2015), ‘Excursion and contour uncertainty regions for latent Gaussian models’, Journal of the Royal Statistical Society: Series B (Statistical Methodology) **77**(1), 85–106.
- Bolin, D. & Wallin, J. (2020), ‘Scale dependence: Why the average CRPS often is inappropriate for ranking probabilistic forecasts’, arXiv preprint arXiv:1912.05642 .
- Brier, G. W. (1950), ‘Verification of forecasts expressed in terms of probability’, Monthly Weather Review **78**, 1–3.
- Chiu, S. N., Stoyan, D., Kendall, W. S. & Mecke, J. (2013), Stochastic Geometry and Its Applications; 3rd ed., Wiley, Hoboken, New Jersey.
- Cui, W. & Perera, A. H. (2008), ‘What do we know about forest fire size distribution, and why is this knowledge useful for forest management?’, International Journal of Wildland Fire **17**(2), 234–244.
- Cumming, S. (2001), ‘A parametric model of the fire-size distribution’, Canadian Journal of Forest Research **31**(8), 1297–1303.

- Davison, A. C. & Smith, R. L. (1990), ‘Models for exceedances over high thresholds (with discussion)’, Journal of the Royal Statistical Society. Series B (Methodological) **52**(3), 393–442.
- De Zea Bermudez, P., Mendes, J., Pereira, J. M., Turkman, K. F. & Vasconcelos, M. J. (2009), ‘Spatial and temporal extremes of wildfire sizes in Portugal (1984–2004)’, International Journal of Wildland Fire **18**(8), 983–991.
- Diggle, P. J., Menezes, R. & Su, T.-I. (2010), ‘Geostatistical inference under preferential sampling (with discussion)’, Journal of the Royal Statistical Society: Series C (Applied Statistics) **59**(2), 191–232.
- Evin, G., Curt, T. & Eckert, N. (2018), ‘Has fire policy decreased the return period of the largest wildfire events in France? A Bayesian assessment based on extreme value theory’, Natural Hazards and Earth System Sciences **18**(10), 2641–2651.
- Fawcett, T. (2006), ‘An introduction to ROC analysis’, Pattern Recognition Letters **27**(8), 861–874.
- Fuglstad, G.-A., Simpson, D., Lindgren, F. & Rue, H. (2018), ‘Constructing priors that penalize the complexity of Gaussian random fields’, Journal of the American Statistical Association **114**(525), 445–452.
- Genton, M. G., Butry, D. T., Gumpertz, M. L. & Prestemon, J. P. (2006), ‘Spatio-temporal analysis of wildfire ignitions in the St Johns River water management district, Florida’, International Journal of Wildland Fire **15**(1), 87–97.
- Gneiting, T. & Ranjan, R. (2011), ‘Comparing density forecasts using threshold- and quantile-weighted scoring rules’, Journal of Business & Economic Statistics **29**(3), 411–422.
- Horvitz, D. G. & Thompson, D. J. (1952), ‘A generalization of sampling without replacement from a finite universe’, Journal of the American Statistical Association **47**(260), 663–685.
- Illian, J. B., Sørbye, S. H. & Rue, H. (2012), ‘A toolbox for fitting complex spatial point process models using integrated nested Laplace approximation (INLA)’, The Annals of Applied Statistics **6**(4), 1499–1530.
- Jones, M. W., Smith, A., Betts, R., Canadell, J. G., Prentice, I. C. & Le Quéré, C. (2020), ScienceBrief Review: Climate change increases the risk of wildfires, in C. Le Quéré, P. Liss & P. Forster, eds, ‘Critical Issues in Climate Change Science’.
- Joseph, M. B., Rossi, M. W., Mietkiewicz, N. P., Mahood, A. L., Cattau, M. E., St. Denis, L. A., Nagy, R. C., Iglesias, V., Abatzoglou, J. T. & Balch, J. K. (2019), ‘Spatiotemporal prediction of wildfire size extremes with Bayesian finite sample maxima’, Ecological Applications **29**(6), e01898.

- Krainski, E. T., Gómez-Rubio, V., Bakka, H., Lenzi, A., Castro-Camilo, D., Simpson, D., Lindgren, F. & Rue, H. (2018), Advanced Spatial Modeling with Stochastic Partial Differential Equations Using R and INLA, Chapman and Hall/CRC.
- Lindgren, F. & Rue, H. (2015), ‘Bayesian spatial modelling with R-INLA’, Journal of Statistical Software **63**(19).
- Lindgren, F., Rue, H. & Lindström, J. (2011), ‘An explicit link between Gaussian fields and Gaussian Markov random fields: The stochastic partial differential equation approach (with discussion)’, Journal of the Royal Statistical Society: Series B (Statistical Methodology) **73**(4), 423–498.
- Lombardo, L., Opitz, T., Ardizzone, F., Guzzetti, F. & Huser, R. (2020), ‘Space-time landslide predictive modelling’, Earth Science Reviews **209**, 103318.
- Lombardo, L., Opitz, T. & Huser, R. (2018), ‘Point process-based modeling of multiple debris flow landslides using INLA: An application to the 2009 Messina disaster’, Stochastic Environmental Research and Risk Assessment **32**(7), 2179–2198.
- Matheson, J. E. & Winkler, R. L. (1976), ‘Scoring rules for continuous probability distributions’, Management Science **22**(10), 1087–1096.
- Mendes, J. M., de Zea Bermudez, P. C., Pereira, J., Turkman, K. F. & Vasconcelos, M. J. (2010), ‘Spatial extremes of wildfire sizes: Bayesian hierarchical models for extremes’, Environmental and Ecological Statistics **17**(1), 1–28.
- Northrop, P. J. & Coleman, C. L. (2014), ‘Improved threshold diagnostic plots for extreme value analyses’, Extremes **17**(2), 289–303.
- Opitz, T. (2017), ‘Latent Gaussian modeling and INLA: A review with focus on space-time applications’, Journal de la Société Française de Statistique **158**(3), 62–85.
- Opitz, T., Bakka, H., Huser, R. & Lombardo, L. (2020), ‘High-resolution Bayesian mapping of landslide hazard with unobserved trigger event’, arXiv preprint arXiv:2006.07902 .
- Opitz, T., Bonneau, F. & Gabriel, E. (2020), ‘Point-process based modeling of space-time structures of forest fire occurrences in Mediterranean France’, Spatial Statistics **40**, 100429.
- Opitz, T., Huser, R., Bakka, H. & Rue, H. (2018), ‘INLA goes extreme: Bayesian tail regression for the estimation of high spatio-temporal quantiles’, Extremes **21**(3), 441–462.
- Peng, R. D., Schoenberg, F. P. & Woods, J. A. (2005), ‘A space-time conditional intensity model for evaluating a wildfire hazard index’, Journal of the American Statistical Association **100**(469), 26–35.

- Pereira, J. M. C. & Turkman, K. F. (2019), Statistical models of vegetation fires: Spatial and temporal patterns, in A. E. Gelfand, M. Fuentes, J. A. Hoeting & R. L. Smith, eds, ‘Handbook of Environmental and Ecological Statistics’, Chapman and Hall/CRC, pp. 401–420.
- Pimont, F., Fargeon, H., Opitz, T., Ruffault, J., Barbero, R., Martin-StPaul, N., Rigolot, E. I., Rivière, M. & Dupuy, J.-L. (2021), ‘Prediction of regional wild-fire activity in the probabilistic Bayesian framework of Firelihood’, Ecological Applications **In press**.
- Preisler, H. K., Brillinger, D. R., Burgan, R. E. & Benoit, J. (2004), ‘Probability based models for estimation of wildfire risk’, International Journal of wildland fire **13**(2), 133–142.
- Raeisi, M., Bonneau, F. & Gabriel, E. (2021), ‘A spatio-temporal multi-scale model for Geyer saturation point process: Application to forest fire occurrences’, Spatial Statistics **41**, 100492.
- Rathbun, S. L. (2013), ‘Optimal estimation of Poisson intensity with partially observed covariates’, Biometrika **100**(1), 277–281.
- Rathbun, S. L., Shiffman, S. & Gwaltney, C. J. (2007), ‘Modelling the effects of partially observed covariates on Poisson process intensity’, Biometrika **94**(1), 153–165.
- Ríos-Pena, L., Kneib, T., Cadarso-Suárez, C., Klein, N. & Marey-Pérez, M. (2018), ‘Studying the occurrence and burnt area of wildfires using zero-one-inflated structured additive beta regression’, Environmental Modelling & Software **110**, 107–118.
- Rue, H., Martino, S. & Chopin, N. (2009), ‘Approximate Bayesian inference for latent Gaussian models by using integrated nested Laplace approximations (with discussion)’, Journal of the Royal Statistical Society: Series B (Statistical Methodology) **71**(2), 319–392.
- Rue, H., Riebler, A., Sørbye, S. H., Illian, J. B., Simpson, D. P. & Lindgren, F. K. (2017), ‘Bayesian computing with INLA: A review’, Annual Review of Statistics and Its Application **4**, 395–421.
- Ruffault, J., Martin-StPaul, N., Pimont, F. & Dupuy, J.-L. (2018), ‘How well do meteorological drought indices predict live fuel moisture content (LFMC)? an assessment for wildfire research and operations in Mediterranean ecosystems’, Agricultural and Forest Meteorology **262**, 391–401.
- Schoenberg, F. P., Peng, R. & Woods, J. (2003), ‘On the distribution of wildfire sizes’, Environmetrics **14**(6), 583–592.
- Serra, L., Juan, P., Varga, D., Mateu, J. & Saez, M. (2013), ‘Spatial pattern modelling of wildfires in Catalonia, Spain 2004–2008’, Environmental Modelling & Software **40**, 235–244.

- Serra, L., Saez, M., Juan, P., Varga, D. & Mateu, J. (2014), ‘A spatio-temporal Poisson hurdle point process to model wildfires’, Stochastic Environmental Research and Risk Assessment **28**(7), 1671–1684.
- Simpson, D., Rue, H., Riebler, A., Martins, T. G., Sørbye, S. H. et al. (2017), ‘Penalising model component complexity: A principled, practical approach to constructing priors’, Statistical Science **32**(1), 1–28.
- Stark, C. P. & Hovius, N. (2001), ‘The characterization of landslide size distributions’, Geophysical Research Letters **28**(6), 1091–1094.
- Stewart, S. I., Radeloff, V. C., Hammer, R. B. & Hawbaker, T. J. (2007), ‘Defining the Wildland–Urban Interface’, Journal of Forestry **105**(4), 201–207.
- Taylor, B. M. & Diggle, P. J. (2014), ‘INLA or MCMC? A tutorial and comparative evaluation for spatial prediction in log-Gaussian Cox processes’, Journal of Statistical Computation and Simulation **84**(10), 2266–2284.
- Tierney, L. & Kadane, J. B. (1986), ‘Accurate approximations for posterior moments and marginal densities’, Journal of the American Statistical Association **81**(393), 82–86.
- Tokdar, S. T. & Kass, R. E. (2010), ‘Importance sampling: A review’, Wiley Interdisciplinary Reviews: Computational Statistics **2**(1), 54–60.
- Tonini, M., Pereira, M. G., Parente, J. & Orozco, C. V. (2017), ‘Evolution of forest fires in Portugal: From spatio-temporal point events to smoothed density maps’, Natural Hazards **85**(3), 1489–1510.
- Turkman, K. F., Amaral Turkman, M. A. & Pereira, J. M. (2010), ‘Asymptotic models and inference for extremes of spatio-temporal data’, Extremes **13**(4), 375–397.
- van Niekerk, J., Bakka, H., Rue, H. & Schenk, L. (2019), ‘New frontiers in Bayesian modeling using the INLA package in R’, arXiv preprint arXiv:1907.10426 .
- van Wagner, C. (1977), ‘Conditions for the start and spread of crown fire’, Canadian Journal of Forest Research **7**(1), 23–34.
- Watanabe, S. (2010), ‘Asymptotic equivalence of Bayes cross validation and Widely Applicable Information Criterion in singular learning theory’, Journal of Machine Learning Research **11**(116), 3571–3594.
- Xi, D. D., Taylor, S. W., Woolford, D. G. & Dean, C. (2019), ‘Statistical models of key components of wildfire risk’, Annual Review of Statistics and Its Application **6**, 197–222.
- Xu, H. & Schoenberg, F. P. (2011), ‘Point process modeling of wildfire hazard in Los Angeles County, California’, The Annals of Applied Statistics **5**(2A), 684–704.

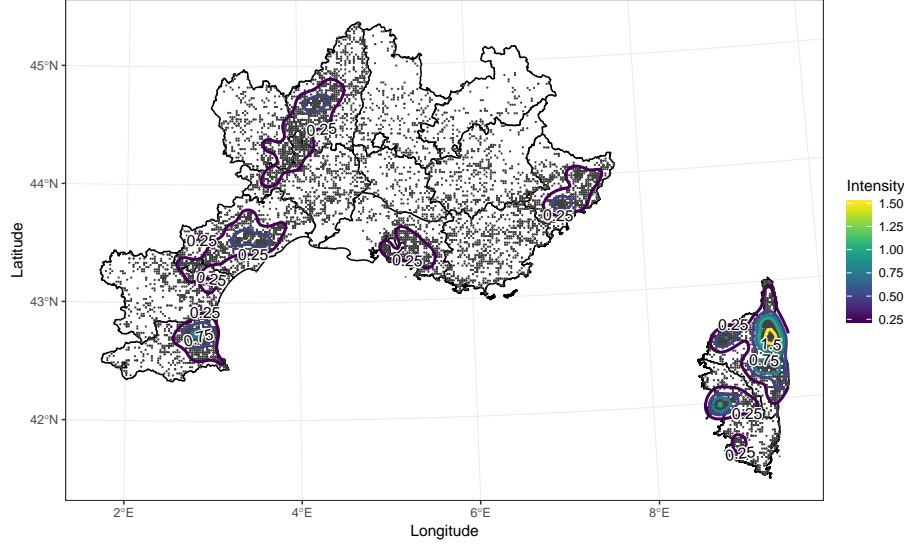


Figure 14: Map of Prométhée data in Southern France with the island of Corsica on the lower right, based on the original DFCI grid used for recording wildfires. Black lines indicate boundaries of administrative regions (“départements”). Coloured lines correspond to intensities (i.e., to average numbers of wildfires per  $\text{km}^2$ ) and highlight areas with many wildfires. Some of the gray points correspond to multiple wildfire occurrences.

## 8 Supplement

### 8.1 Kernel intensity plot

Figure 14 shows a map of the wildfire locations as recorded in the Prométhée database. The overlaid contour lines of a kernel intensity estimation highlight the strong spatial nonstationarity, with several relatively small hotspot areas characterized by high occurrence numbers.

### 8.2 Mean excess plots

We consider the mean excess plots of burnt areas and  $\log_{10}$  burnt areas in the middle and right displays of Figure 15. Given a threshold value  $u$  set for a random variable  $Y$ , the mean excess corresponds to the conditional expectation  $\mathbb{E}[Y - u \mid Y > u]$ , i.e., the expectation of the positive excess above the threshold. Mean excess plots report the corresponding empirical means. In case of exponential tail decay  $\Pr(Y > y) = \exp\{-(y - \mu)/\lambda\}$  for  $y \geq u_0$  with scale  $\lambda > 0$  and an arbitrary shift  $\mu \in \mathbb{R}$ , the mean excess would be constant  $\lambda$  for thresholds  $u$  above  $u_0$ . The mean excess plot for  $\log_{10}$  of BA- $\log_{10}$  indicates

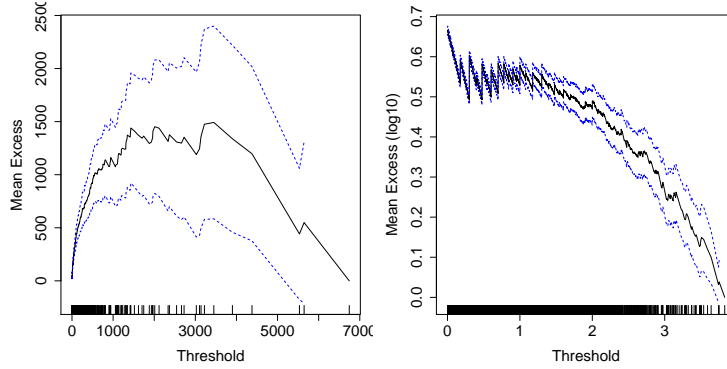


Figure 15: Mean excess plots. Left: for burnt areas (in ha). Right: for  $\log_{10}$  of burnt areas. Original observations are indicated at the bottom of the mean excess plots. Blue lines indicate symmetric pointwise confidence intervals at 95%.

approximately exponential tail decay for low thresholds where mean excess values are relatively stable for threshold values in  $(0, 1.5)$  except for rounding of burnt areas. However, the tail decay becomes faster at higher levels, starting at around 30 ha. Exponential decay on log-scale would correspond to power-law decay at the original scale; i.e., to Pareto-like behavior. By contrast, the mean excess plot of original BA values becomes relatively stable for thresholds above 500 ha, such that the true, ultimate tail decay rate at very high quantiles could be exponential. These plots reveal the difficulty of choosing an appropriate probability distribution for burnt areas.

### 8.3 Subsampling experiments

We implement several experiments to aid the choice of the parameters of the subsampling scheme detailed in §3.4. We fix the sampling probability parameter to  $p_{SS} = 0.9$  but allow the empirical FWI probability  $p_{FWI}$  to equal  $\{0.1, 0.3, 0.5, 0.7, 0.9\}$ . The case  $p_{SS} = 1 - p_{FWI}$ , i.e.,  $p_{FWI} = 0.1$ , corresponds to uniform subsampling, whereas higher values of  $p_{FWI}$  include a relatively larger number of high FWI observations in the subsample.

In a first simulation experiment, we sample from the COX model with log-linear intensity in §4.1,

$$\mu_{i,t}^{COX} = \alpha + \beta_1 z_{FWI}(s_i, t) + \beta_2 m(t),$$

with  $\alpha = -11$ ,  $\beta_1 = 0.15$  and  $\beta_2 = 0.1$  to reflect intensities that could be realistic in a wildfire application, and fit this model with INLA. Figure 16 highlights the improvement in estimation quality by moving away from uniform subsampling, with lower root mean squared errors of the posterior means.

In another experiment, we estimated the COX model with the linear predictor in §4.3 and evaluated the sCRPS scores for the annually aggregated predicted



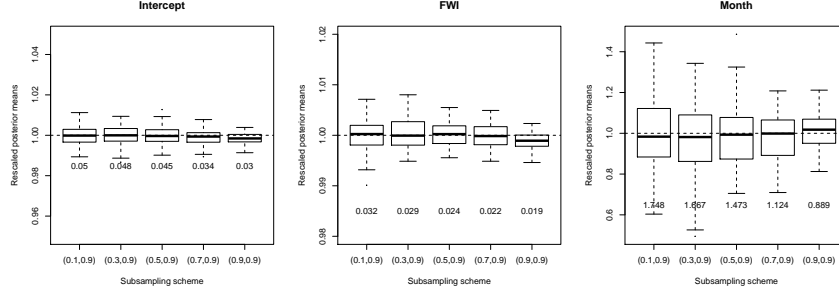


Figure 16: Boxplots of posterior means (rescaled by dividing them by the true parameter value) of fixed effect coefficients from 100 simulations with different  $(p_{FWI}, p_{SS})$  combinations. The relative root mean square errors (rRMSE) for each subsampling scheme are displayed below the corresponding boxplots.

and observed number of fires over the whole spatial region in the training set with 500 posterior simulations and 50 different subsampling seeds. The left panel of Figure 17 shows that subsampling scheme with  $(p_{FWI}, p_{SS}) = (0.7, 0.9)$  achieves the best score. Next, we repeated the experiment with a fixed  $p_{FWI}$  and  $p_{SS}$ , but increased the number of subsamples taken within each pixel-year. The right panel of Figure 17 shows that there is little improvement in sCRPS score beyond two subsamples per pixel-year, while the computational time and memory requirements increase strongly non-linearly with the number of subsamples (not shown).

## 8.4 Other hyperpriors

To all fixed effect coefficients in our models (e.g.,  $\alpha^{COX}$ ,  $\alpha^{BIN}$ ,  $\alpha^{GPD}$  and  $\alpha^{BETA}$ ), we assign flat Gaussian priors with zero mean and precision 0.001. The prior for each of the scaling parameters  $\beta^{COX-BET}$ ,  $\beta^{COX-BIN}$  and  $\beta^{BIN-GPD}$  is a zero-centered Gaussian distribution with precision 1/20. To reduce the number of estimated hyperparameters, we fixed the hyperparameters associated with the priors  $\mathcal{GP}_{1D-SPDE}$  to values guided by prior knowledge about the relationship between FWI/FA and the relevant aspects of wildfire risk. Lastly, we assign a log-Gamma hyperprior with mean unity and precision 0.0005 to each of the random-walk hyperparameters  $\tau_1$ ,  $\tau_2$ ,  $\tau_3$ ,  $\tau_4$ ,  $\tau_5$ ,  $\tau_6$  and  $\tau_7$ .

## 8.5 Empirical distribution of sCRPS, CRPS and twCRPS

Figure 18 shows the empirical distributions of sCRPS, CRPS and twCRPS for model M1 compared to M2, M4 and M5.

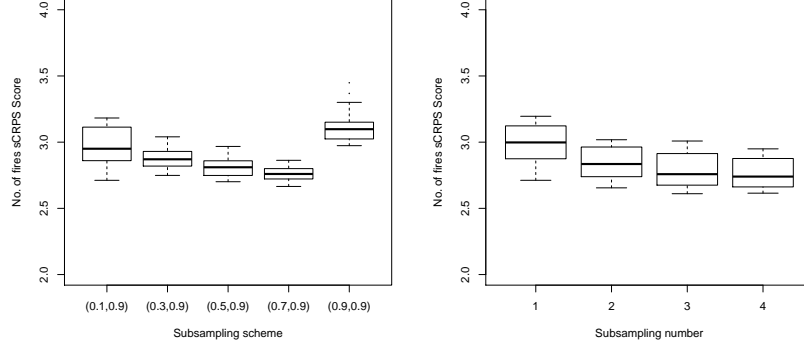


Figure 17: sCRPS for the annually aggregated predicted and observed number of fires over the whole spatial region in the training set (1994–2014), with the subsampling scheme over 50 different seeds. Right: Boxplots of sCRPS scores for the subsampling scheme with one subsample per pixel-year and different  $(p_{FWI}, p_{SS})$  combinations. Left: Boxplots of sCRPS scores for the subsampling with  $(p_{FWI}, p_{SS})=(0.1,0.9)$ , with different number of subsamples per pixel-year.

## 8.6 Spatial effects in model M1

Figure 19 shows the same plot as Figure 12 but for the shared spatial random field  $g^{\text{BIN-GPD}}$ .

Figure 20 shows the posterior means of all the spatial model M1, with priors detailed in §4.3.

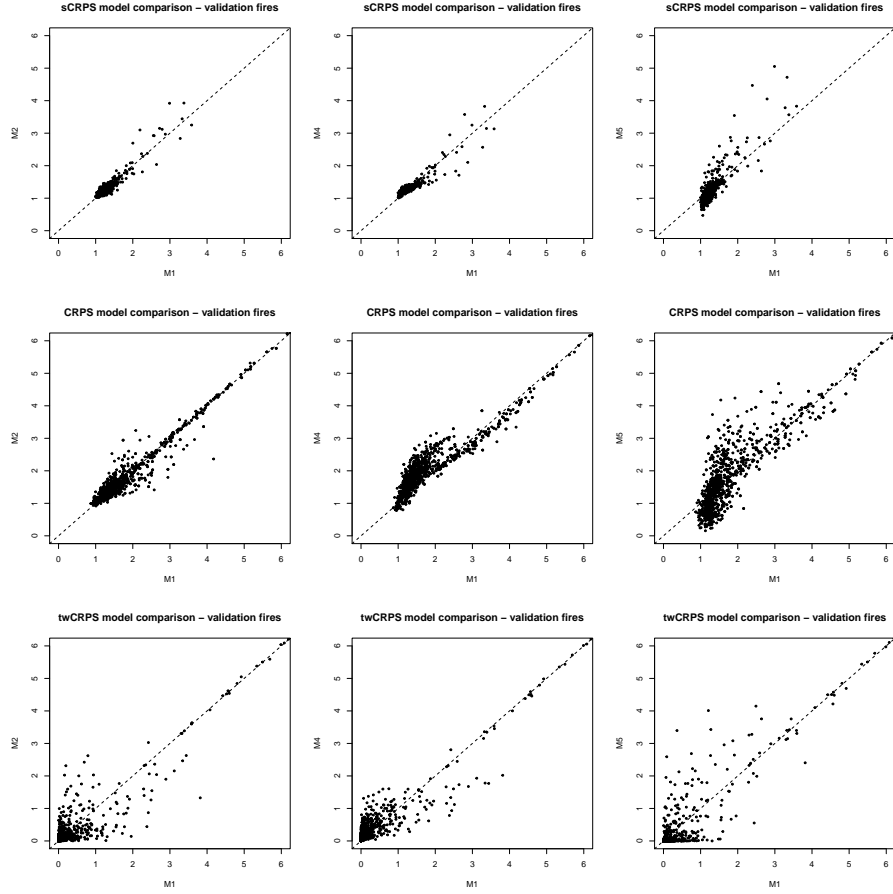


Figure 18: Log-log plots for the empirical sCRPS (top), CRPS (middle) and twCRPS (bottom) for the model M1 with respect to the model M2 (left), M4 (center) and M5 (right).

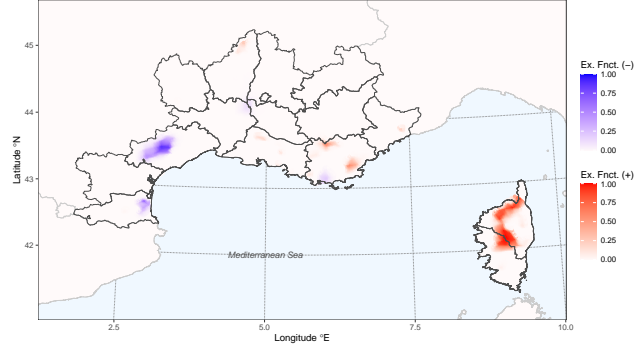


Figure 19: Excursion functions of posterior latent fields above  $u = 0.1$  and below  $-u$ . Plots show  $\max\{F_{0.1}^+(\cdot), F_{0.1}^-(\cdot)\}$  for the shared spatial random field  $g^{\text{BIN-GPD}}$ .

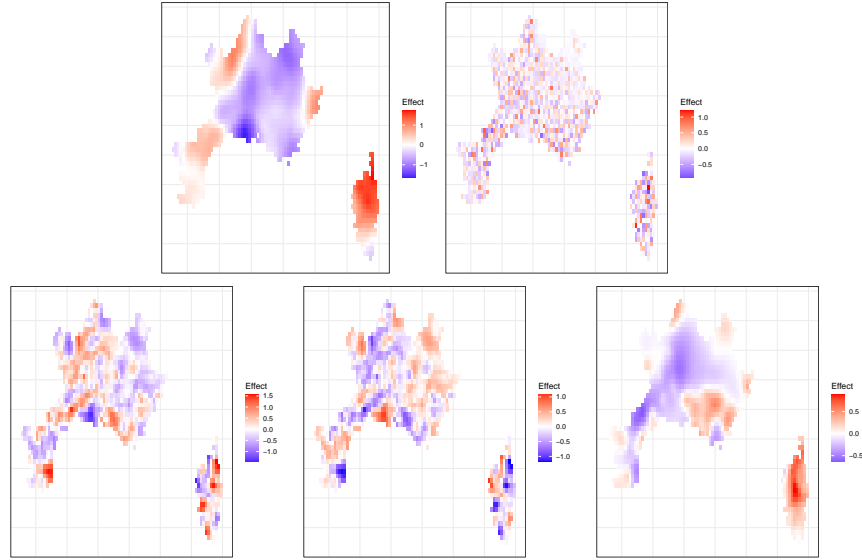


Figure 20: Posterior means of (top left to bottom right):  $\beta^{\text{COX-BETA}} g^{\text{COX-BET}}(\cdot)$ ,  $g_1^{\text{COX}}(\cdot)$ ,  $\beta^{\text{COX-BIN}} g^{\text{COX-BIN}}(\cdot)$ ,  $g^{\text{COX-BIN}}(\cdot)$  and  $\beta^{\text{BIN-GPD}} g^{\text{BIN-GPD}}(\cdot)$  effects in the model.